



UNIVERSITY OF LEEDS

This is a repository copy of *Selective Photocatalytic Activities of Amino Acids/Peptide-Ti₃C₂T_x-TiO₂ Composites Induced by Calcination: Adsorption Enhancement vs Charge Transfer Enhancement*.

White Rose Research Online URL for this paper:

<https://eprints.whiterose.ac.uk/202213/>

Version: Accepted Version

Article:

Zhang, H., Yao, J., Zhang, X. et al. (5 more authors) (2023) Selective Photocatalytic Activities of Amino Acids/Peptide-Ti₃C₂T_x-TiO₂ Composites Induced by Calcination: Adsorption Enhancement vs Charge Transfer Enhancement. *Journal of Physical Chemistry C*, 127 (5). pp. 2231-2245. ISSN 1932-7447

<https://doi.org/10.1021/acs.jpcc.2c08427>

© 2023 American Chemical Society. This is an author produced version of an article published in *Journal of Physical Chemistry C*. Uploaded in accordance with the publisher's self-archiving policy.

Reuse

Items deposited in White Rose Research Online are protected by copyright, with all rights reserved unless indicated otherwise. They may be downloaded and/or printed for private study, or other acts as permitted by national copyright laws. The publisher or other rights holders may allow further reproduction and re-use of the full text version. This is indicated by the licence information on the White Rose Research Online record for the item.

Takedown

If you consider content in White Rose Research Online to be in breach of UK law, please notify us by emailing eprints@whiterose.ac.uk including the URL of the record and the reason for the withdrawal request.



eprints@whiterose.ac.uk
<https://eprints.whiterose.ac.uk/>

Selective Photocatalytic Activities of Amino Acids/Peptide-Ti₃C₂T_x-TiO₂ Composites Induced by Calcination: Adsorption Enhancement Versus Charge Transfer Enhancement

Hui Zhang^{a, b, *}, Jiale Yao^{a, b}, Xinyue Zhang^c, Chengyu Fu^{a, b}, Yaping Miao^b, Yani Guo^c, Zhi Tong^c, Ningtao Mao^{d, *}

^a School of Textile Science & Engineering, Xi'an Polytechnic University, Xi'an, Shaanxi 710048, PR China

^b Key Laboratory of Functional Textile Material and Product (Xi'an Polytechnic University), Ministry of Education, Xi'an, Shaanxi 710048, PR China

^c School of Environmental and Chemical Engineering, Xi'an Polytechnic University, Xi'an, Shaanxi 710048, PR China

^d School of Design, University of Leeds, Leeds, LS2 9JT, United Kingdom

* Email: hzhangw532@xpu.edu.cn (H. Zhang); n.mao@leeds.ac.uk (N. Mao)

ABSTRACT: A ternary component composite composed of amino acids/peptide, $\text{Ti}_3\text{C}_2\text{T}_x$ and TiO_2 was fabricated by incorporating peptide chains of wool keratin between $\text{Ti}_3\text{C}_2\text{T}_x$ nanosheets and TiO_2 nanoparticles based on the low-temperature vibration-assisted grinding process and hydrothermal synthesis method. The as-obtained amino acid/peptide- $\text{Ti}_3\text{C}_2\text{T}_x$ - TiO_2 (P-T-T) composite was further calcined under nitrogen gas condition. The photocatalytic properties of the control $\text{Ti}_3\text{C}_2\text{T}_x$ - TiO_2 (T-T), P-T-T, and calcined P-T-T (CP-T-T) composites were evaluated for the photodegradation of C.I. Reactive Blue 194 dye, tetracycline hydrochloride and levofloxacin antibiotics. First principles calculations were performed to verify the experimental results. It was concluded that in comparison with the T-T and P-T-T composites, the CP-T-T composite had an excellent photocatalytic activity for the decomposition of C.I. Reactive Blue 194. This was ascribed to the large BET specific surface area, the presence of micropores and mesopores, the narrowed band gap with an internal electric field (IEF), and the intimate contacts among peptide, $\text{Ti}_3\text{C}_2\text{T}_x$ and TiO_2 , which resulted in the fast transfer and separation of charge carriers in the composite. The photodegradation pathways of C.I. Reactive Blue 194 dye by the P-T-T and CP-T-T composites were different. The peptide chains of wool keratin led to the redistribution of the electron accumulation and depletion on the peptide, $\text{Ti}_3\text{C}_2\text{T}_x$ and TiO_2 , which changed the direction of IEF in the composite. Interestingly, the adsorption-mediated photocatalytic degradation of C.I. Reactive Blue 194 by the P-T-T composite was transformed to the charge transfer-mediated photocatalytic degradation of the same dye by the CP-T-T composite.

KEYWORDS: wool keratins, amino acids, photocatalysis, adsorption, charge transfer

INTRODUCTION

MXenes are regarded as promising co-catalysts and have unique layered hexagonal structures, elemental compositions, and surface termination groups, and thus lead to intriguing mechanical, physical, chemical, and electronic characteristics.¹ Among them, $\text{Ti}_3\text{C}_2\text{T}_x$ MXene can not only act as the electron acceptor to promote the separation of charge carriers, but also provides abundant active sites.² $\text{Ti}_3\text{C}_2\text{T}_x$ -derived photocatalysts, such as $\text{Ti}_3\text{C}_2\text{T}_x/\text{In}_2\text{S}_3/\text{TiO}_2$,³ black phosphorus/ $(\text{Ti}_3\text{C}_2\text{T}_x@\text{TiO}_2)$,⁴ and $\text{BiOBr}/(001)\text{-TiO}_2/\text{Ti}_3\text{C}_2\text{T}_x$,⁵ have been fabricated through different processing techniques.⁶ The role of $\text{Ti}_3\text{C}_2\text{T}_x$ in composite photocatalysts has been extensively explored. The conductive $\text{Ti}_3\text{C}_2\text{T}_x$ can effectively accelerate the migration and separation of photo-induced charge carriers in $\text{BiOBr}/\text{TiO}_2/\text{Ti}_3\text{C}_2\text{T}_x$ ⁷ and $\text{TiO}_2/\text{Ti}_3\text{C}_2\text{T}_x/\text{AgI}$.⁸ The content of $\text{Ti}_3\text{C}_2\text{T}_x$ in the binary composite photocatalyst $\text{Ti}_3\text{C}_2\text{T}_x/\text{TiO}_2$ has vital effect on its photocatalytic activity.⁹ The Ti vacancy sites can stabilize the defective structure, while the oxygen vacancy sites are helpful for the activation of O_2 to recover lattice oxygen.¹⁰ More hydroxyl radicals can be generated from the few-layer $\text{Ti}_3\text{C}_2\text{T}_x$ nanosheets as compared with the multi-layer $\text{Ti}_3\text{C}_2\text{T}_x$ nanosheets, and the high photocatalytic activity is attributed to its higher content of active TiO_2 sites, resulting in more redox reaction sites.¹¹ It is demonstrated that the internal electric field (IEF) of heterojunction promotes the transfer of photogenerated electrons to Ti_3C_2 from TiO_2 , and the amount of heterojunction affects the migration of photogenerated electrons.^{12,13} The $\text{Ti}_3\text{C}_2\text{T}_x$ -generated plasmonic electrons are transferred into the conduction band of TiO_2 over the Schottky barrier, and the strong electronic coupling between oxygen-terminated $\text{Ti}_3\text{C}_2\text{T}_x$ and TiO_2 is ascribed to their proximity.¹⁴

Although protein materials have the low chemical resistance and are liable to photodegradation, a good compatibility of TiO_2 and wool keratin composed by amino acids/peptide has been recognized.¹⁵ The S and N elements of wool keratin can be doped with TiO_2 to improve the visible light induced photocatalytic activity of

TiO₂-coated wool fibers.¹⁶ It has been verified that the type of amino acids affects not only the adsorption and photocatalytic oxidation of amino acids adsorbed on TiO₂ surface,¹⁷ but also the recombination rate of photogenerated charge carriers of C, N and S co-doped TiO₂.¹⁸ For example, the adsorption of serine and histidine amino acids on TiO₂ surface is helpful for the ligand-to-metal charge transfer between amino acids and TiO₂ to activate peroxymonosulfate to produce sulfate radicals,¹⁹ and the histidine-modified TiO₂ can accelerate the electron transfer from TiO₂ to Zn²⁺, Pb²⁺ and Cu²⁺ ions through the imidazole bridge.²⁰ Similarly, the high activity TiO₂ can be prepared by using branched amino acids, such as proline, valine, and aspartic acids, for the photodegradation of methylene blue and calmagite dyes.²¹ The charge transfer and subsequent deprotonation are existed in the photodegradation process of aromatic amino acids like histidine, tyrosine, and tryptophan.²² Additionally, the peptide can not only promote the transfer of photoinduced electrons in the Eosin Y/Pt/peptide composite film,²³ but also enhance the photocatalytic and electrical properties of TiO₂.²⁴

Generally, the photocatalytic reaction process involves three steps. Firstly, the light excites the catalysts to produce the photo-generated charge carriers. Secondly, the carriers are isolated and transferred to catalyst surface. At last, the carrier induces the redox reactions on catalyst surface.²⁵ The photocatalytic activity of photocatalysts depend upon not only the separation and transfer of photogenerated charge carriers,²⁶ but also their adsorption capability towards pollutants.²⁷ However, there is hardly any studies on the selective photocatalytic activity of composite photocatalysts via either mediating the pollutant adsorption or the charge transfer. In order to clarify the effects of both pollutant adsorption enhancement and charge transfer enhancement on the photocatalytic activity of Ti₃C₂T_x-based photocatalysts, we conceptualized a novel wool keratin amino acids/peptide-Ti₃C₂T_x-TiO₂ (P-T-T) composite photocatalyst to degrade organic reactive dye pollutants. Both P-T-T and calcinated P-T-T (CP-T-T) composites were developed by using various amounts of amino acids/peptide of wool keratin in

relation to the amounts of $\text{Ti}_3\text{C}_2\text{T}_x$ and TiO_2 in the composite. Their photocatalytic properties were evaluated by employing reactive dye containing two different active groups as the photocatalytic degradation model of pollutants. It was believed that the photoinduced reactive species with varying degrees of activities might attack different active groups of dye to produce a range of different intermediate products. The impacts of the peptide of wool keratin on the adsorption or electron transfer between $\text{Ti}_3\text{C}_2\text{T}_x$ and TiO_2 in the P-T-T composite were investigated. In addition, the first-principles theoretical calculations were employed to validate the effect of charge transfer on this photocatalytic property of P-T-T composite.

METHODS

Experimental Section. The detailed information about materials and chemicals used in this work was described in Supporting Information S1. Figure 1 shows the schematic for the fabrication of P-T-T composite. The wool flakes were prepared by vibration-assisted grinding process at low temperature. The $\text{Ti}_3\text{C}_2\text{T}_x$ nanosheets were prepared through acid etching, ball milling and ultrasonic exfoliation processes. The detailed procedures for preparation of wool flakes and few-layered $\text{Ti}_3\text{C}_2\text{T}_x$ nanosheets were separately described in Supporting Information S2 and S3. The P-T-T composite was fabricated by a hydrothermal method. In a typical case, according to the optimized mass ratio of wool flakes to $\text{Ti}_3\text{C}_2\text{T}_x$ 1:4, the wool flakes were first mixed with the few-layered $\text{Ti}_3\text{C}_2\text{T}_x$ nanosheets, and then ground by the ball milling process at $-40\text{ }^\circ\text{C}$ for 15 min to gain the intercalated peptide- $\text{Ti}_3\text{C}_2\text{T}_x$ hybrid particles. Next, 1.0 mL of TBT was added in 40 mL of absolute alcohol under magnetic stirring at room temperature, and 0.1 g of the peptide- $\text{Ti}_3\text{C}_2\text{T}_x$ particles (or $\text{Ti}_3\text{C}_2\text{T}_x$ nanosheets) was then added. 40 mL of deionized water was subsequently added into the above mixture solution under vigorous stirring. The mixed solution with a pH value of 6.8 was immediately transferred to a 100 mL PTFE reaction tank, which was sealed in a stainless-steel autoclave. After that, the autoclave was placed in a reactor and run at a speed

of 10 revolution per minute. At the same time, the autoclave was heated to 120 °C and then maintained at the constant temperature for 3 h. When the autoclave cooled down naturally to ambient temperature, the as-synthesized precipitates were collected by centrifugation and washed repeatedly with absolute ethanol and deionized water till the pH value of the solution was 7. The amino acid compositions of wool keratins could be maintained to great extent despite the reaction was carried out in hot water and absolute alcohol at high pressure.²⁸ Lastly, the as-prepared P-T-T (or T-T as the control) composite particles were dried in the lyophilier. In addition, the P-T-T composite was calcined at 400 °C for 2 h in nitrogen atmosphere to carbonize/modify amino acids (peptide) of wool keratins.

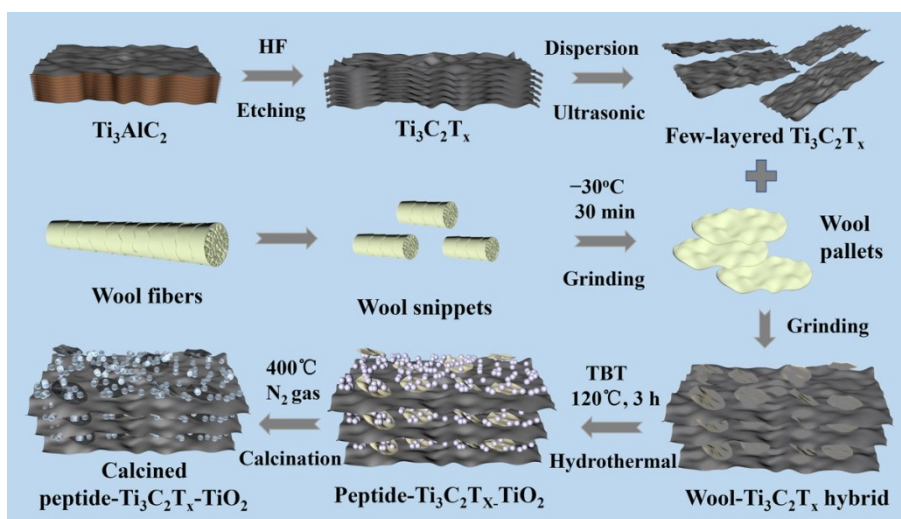


Figure 1. The schematic illustration for fabrication of P-T-T composite.

The characterization techniques including field-emission scanning electron microscopy (FESEM), atomic force microscope (AFM), X-ray diffraction (XRD), Brunauer-Emmett-Teller (BET) adsorption isotherm, transmission electron microscopy (TEM), X-ray photoelectron spectroscopy (XPS), diffuse reflectance spectroscopy (DRS), ultraviolet (UV) photoelectron spectroscopy (UPS), zeta potential, photoluminescence (PL) spectroscopy, electrochemical impedance spectra (EIS), photocurrent, electron paramagnetic resonance (EPR)

and electron spin resonance (ESR) spectra, amino acid contents, and organic elemental analysis were described in Supporting Information S4.

The photocatalytic activities of the T-T, P-T-T, and CP-T-T composites were evaluated by using the C.I. Reactive Blue 194 dye as the photodegradation model exposure to visible light. Prior to usage, the C.I. Reactive Blue 194 dye was purified and the detailed procedure was described in Supporting Information S5. A 300 W Xenon lamp with a 420-780 nm bandpass filter was used as the visible light source, and the optical power density was measured to be 1.30 W/cm². In a typical experiment, 0.2 g of the specimens were dispersed in a quartz tube containing 30 mL of 20 mg/L dye solution under continuous stirring for 40 min to reach the adsorption-desorption equilibrium in darkness. After that, the mixture solution was irradiated with the Xenon lamp. At the specific interval, the lamp was shielded off and about 5 mL of the testing solution was taken from the suspension and then centrifugated at 11000 revolution per minute for 10 min. The supernatant was extracted from the dye solution and its spectrophotometric analysis was conducted on a T2602 spectrophotometer (Shanghai Youke Instrument Co., Ltd, Shanghai, China). Its absorbance was measured at the maximum absorption wavelength of 602 nm. After the measurement, the dye solution along with the particles was added back to the mixture solution which was irradiated with the lamp. The concentration (C_t) of the dye solution was calculated according to the standard working equation ($A_t=0.00871+0.02251C_t$, $R^2=0.999$). The removal efficiency (E_A) (or degradation efficiency, E_D) was calculated using the equation (1):

$$E_A(\text{or } E_D)=(1-C_t/C_0)\times 100 \quad (1)$$

where C_0 and C_t were separately the concentrations of dye solution at the initial time and any given time t . According to the Langmuir-Hinshelwood model,²⁹ the apparent photodegradation rate constant (k value) of the dye solution was calculated using the equation (2):

$$\ln(C_t/C_0) = -k \times t \quad (2)$$

The photodegradation products were analyzed using the high-performance liquid chromatography (HPLC) system coupled with a mass spectrometer (MS), and the detailed procedure was described in Supporting Information S6. Furthermore, the photodegradation behaviors of the tetracycline hydrochloride (TC-HCl) and levofloxacin (LFX) aqueous solutions by the as-prepared composites were assessed under visible light based on the above-mentioned method. An appropriate number of composite particles (20 mg) was dispersed in 50 mL of 20 mg/L TC-HC (or 5 mg/L LFX) aqueous solution. The absorbances were measured at the maximum absorption wavelengths of 356 nm for TC-HCl and 287 nm for LFX. The corresponding concentrations were calculated according to the standard working equations (TC-HCl: $A_t = 0.02894 + 0.02933C_t$, $R^2 = 0.998$ and LFX: $A_t = 0.016 + 0.0677C_t$, $R^2 = 0.999$). The average values of E_A , E_D and k were obtained in triplicates using the Equations (1) and (2).

First Principles Calculations. The detailed first principles calculations for the T-T and P-T-T composites were described in Supporting Information S7 according to the density functional theory (DFT). Due to the limitation of computing capacity, the two amino acids (methionine and isoleucine) of wool keratins which have the highest contents were assumed to form a peptide chain to combine with $Ti_3C_2T_x$ and TiO_2 unit cells.

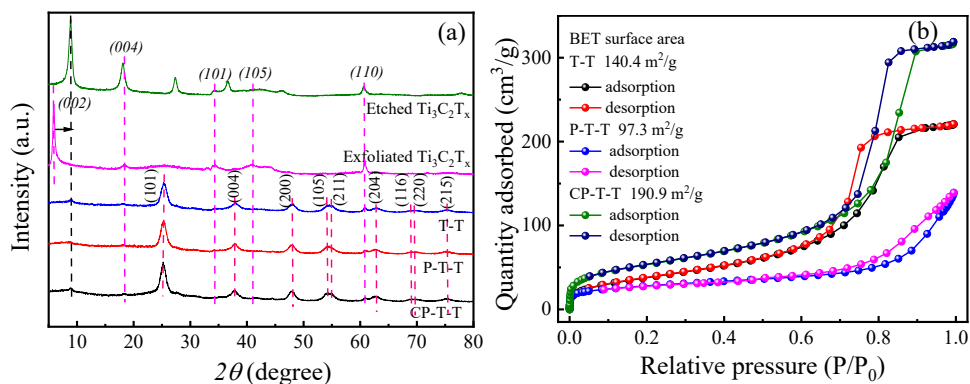
RESULTS AND DISCUSSION

Structural Characterizations of the Resultant Products. All the as-prepared products have the irregular shapes dotted with the multi-hierarchy pores and crevices, and their particle sizes are within the micro-meter range (Figure S1). The high-magnified FESEM images indicate that they are covered by a layer of sub-micro- and nano-scaled particles. The lamellar wool particles are obtained when wool fibers are processed by vibration-assisted grinding at low temperature (Figure S1a). After HF etching, the bulk Ti_3AlC_2 particles is transformed

into the multi-layered $\text{Ti}_3\text{C}_2\text{T}_x$ particles with the stratification and accordion-like structure (Figure S1b), implying the removal of Al layers from $\text{Ti}_3\text{C}_2\text{T}_x$.³⁰ After exfoliation, the height profile and AFM image (Figure S1c) verify that the average thickness of the exfoliated $\text{Ti}_3\text{C}_2\text{T}_x$ nanosheets is 2.8 nm equal to about three layers.³¹ The $\text{Ti}_3\text{C}_2\text{T}_x$ - TiO_2 (T-T) composite exhibits the lamellar feature of $\text{Ti}_3\text{C}_2\text{T}_x$ (Figure S1d and S1e). Nevertheless, the layer-structured $\text{Ti}_3\text{C}_2\text{T}_x$ is not found in both of the P-T-T (Figure S1f and S1g) and CP-T-T (Figure S1h and S1i) mainly due to the blending of wool with $\text{Ti}_3\text{C}_2\text{T}_x$ and the coating of TiO_2 .

Figure 2a shows the XRD patterns of the as-prepared products. The typical diffraction peaks of $\text{Ti}_3\text{C}_2\text{T}_x$ nanosheets at 6.0° , 18.5° , 34.4° , 41.0° and 60.8° are identified, which correspond to the (002), (004), (101), (105) and (110) crystal planes of $\text{Ti}_3\text{C}_2\text{T}_x$, respectively.³² The strongest diffraction peak at the (002) plane is downshifted from about 9° to 6° when the multi-layer $\text{Ti}_3\text{C}_2\text{T}_x$ particles are successfully exfoliated into the few-layer $\text{Ti}_3\text{C}_2\text{T}_x$ nanosheets.³³ After being loaded with TiO_2 nanoparticles under hydrothermal condition, the characteristics peaks of TiO_2 at 25.4° , 38.0° , 48.0° , 54° , 55° , 63° , 69° , 70° and 75° are detected on the $\text{Ti}_3\text{C}_2\text{T}_x$ @ TiO_2 (T-T) composite, which are indexed to the (101), (004), (200), (105), (211), (204), (116), (220) and (215) planes of anatase phase TiO_2 (JCPDS no.21-1272), respectively.³⁴ Meanwhile, the diffraction peaks of $\text{Ti}_3\text{C}_2\text{T}_x$ nanosheets at the (004), (101), (105) and (110) planes are observed, but their intensities decrease to some degrees because of the presence of TiO_2 . Moreover, the major diffraction peak at 6.0° is disappeared. On the contrary, a weak diffraction peak at around 9.0° is formed, which is probably attributed to the incorporation of TiO_2 nanoparticles into the inter-layers of $\text{Ti}_3\text{C}_2\text{T}_x$, resulting in the stack of $\text{Ti}_3\text{C}_2\text{T}_x$ nanosheets coated with TiO_2 nanoparticles. For both P-T-T and CP-T-T composites, there are no significant changes in their XRD patterns as compared with the control T-T composite. It means that the introduction of wool keratins has no influences on the crystal structure of T-T, and the calcination process at 400°C in nitrogen gas does not alter the crystal

structures of $\text{Ti}_3\text{C}_2\text{T}_x$ and TiO_2 . Figure 2b to 2d show the nitrogen adsorption-desorption isotherms, pore volume and pore area distribution curves of the products. According to the international union of pure and applied chemistry (IUPAC) standard, the T-T, P-T-T and CP-T-T composites possess the typical IV adsorption behaviors along with the H3 hysteresis loop in $0.6 < P/P_0 < 1.0$ region (Figure 2b), suggesting the coexistence of micropores and mesopores.³⁰ The specific surface area of the T-T composite is measured to be $140.4 \text{ m}^2/\text{g}$ based on Brunauer-Emmett-Teller (BET) method. When the wool flakes are introduced, the BET specific surface area of the P-T-T composite decreases to $97.3 \text{ m}^2/\text{g}$, but increases to $190.9 \text{ m}^2/\text{g}$ after its calcination in nitrogen atmosphere. The increased specific surface area of the CP-T-T composite is probably induced by the formation of active carbon micropores and mesopores during the calcination of wool keratin in the composite. This is demonstrated by the pore volume distribution curves versus the Barrett-Joyner-Halenda (BJH) pore sizes (Figure 2c). Additionally, the pore volume and pore area distribution curves indicate that the large pore volume and pore area of the CP-T-T composite will provide more active sites for the photodegradation or photoreduction reaction of adsorbed pollutants (Figure 2d).



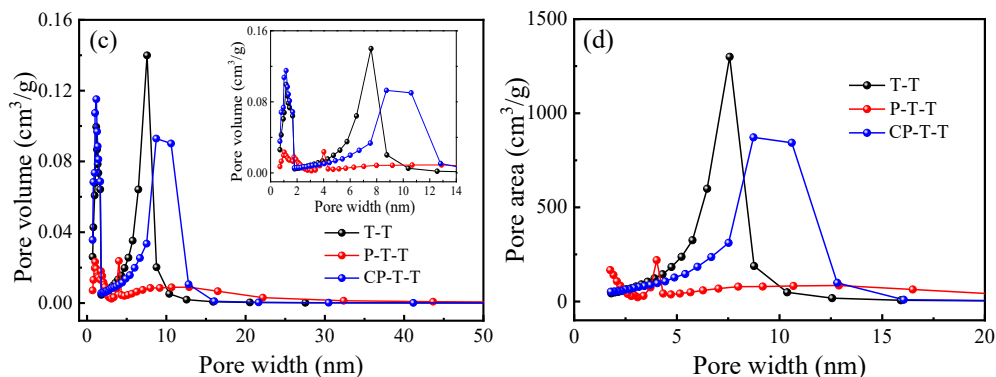


Figure 2. The (a) XRD patterns, (b) nitrogen adsorption–desorption isotherms, (c) pore volume and (d) pore area distribution curves of as-prepared products.

The P-T-T composite is composed of wool flakes (bright areas) and $\text{Ti}_3\text{C}_2\text{T}_x$ sheets (dark areas) in the low-resolution TEM image (Figure 3a). The fishbone-like $\text{Ti}_3\text{C}_2\text{T}_x$ sheets are separated from each other by wool flakes, and the thickness of $\text{Ti}_3\text{C}_2\text{T}_x$ sheets is in the sub-micrometer scales (Figure 3b). Many nano-scaled particles are embedded into the interior of peptide- $\text{Ti}_3\text{C}_2\text{T}_x$ (P-T) in some areas (Figure 3c). The high-resolution TEM image (Figure 3d) confirms the existence of laminar $\text{Ti}_3\text{C}_2\text{T}_x$ with a single layer thickness of 1.01 nm corresponding to the (002) plane of $\text{Ti}_3\text{C}_2\text{T}_x$.¹⁴ Moreover, a few spherical nanoparticles are tightly connected with $\text{Ti}_3\text{C}_2\text{T}_x$ nanosheets, and its inter-planar distance of 0.346 nm is ascribed to the (101) plane of anatase TiO_2 .³³ For the CP-T-T composite, it is consisting of layered agglomerates (Figure 3e), which are made up of the multi-layer $\text{Ti}_3\text{C}_2\text{T}_x$ mixed with organic components (Figure 3f). Similarly, a few nanoparticles are incorporated into the interlayer of $\text{Ti}_3\text{C}_2\text{T}_x$ nanosheets (Figure 3g), and the inter-planar distance of the as-synthesized nanoparticles is measured to be 0.342 nm, corresponding to the (101) plane of anatase TiO_2 (Figure 3h). Therefore, the intimate contact between $\text{Ti}_3\text{C}_2\text{T}_x$ and TiO_2 is formed to facilitate the transfer and separation of charge carriers in the photocatalytic reaction process.

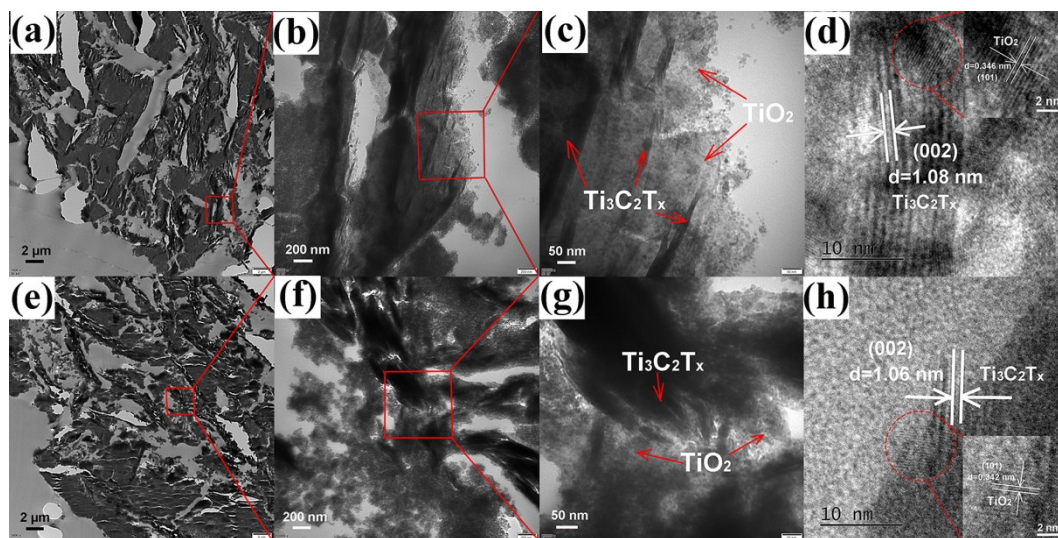


Figure 3. The TEM images of (a) to (d) P-T-T and (e) to (h) CP-T-T composites.

Figure S2 and Table S1 show the XPS spectra and analysis data of the products. The T-T composite includes the elements of C, F, O and Ti, and the F element is caused by the residual of HF used. When wool flakes are introduced, besides the C, F, O and Ti elements, N and S elements are found in the P-T-T composite. After calcination, F and S elements disappeared in the CP-T-T composite surface probably because of the high temperature annealing effects in nitrogen atmosphere, and the elements of C, N, O and Ti are left. For the T-T composite (Figure S2b1 to S2b4), the C1s core-level XPS spectrum can be fitted into five subpeaks of C-F, C-O, C-C, O_x-C-Ti, and C-Ti at the binding energies of 288.75, 286.49, 284.78, 283.17, and 281.25 eV, respectively.³¹ The F1s XPS spectrum has only the F-C subpeaks at the binding energy of 684.66 eV. The O1s XPS spectrum is fitted into four subpeaks of O-H, O-C, O-Ti, and O_x-Ti-C at the binding energies of 533.57, 532.32, 530.43, and 528.01 eV, respectively.³⁵ The Ti2p XPS spectrum is fitted into six subpeaks of O_x-Ti2p_{1/2}-C, O_x-Ti2p_{3/2}-C, Ti2p_{1/2}-O, Ti2p_{3/2}-O, Ti2p_{1/2}-C, and Ti2p_{3/2}-C, corresponding to the binding energies of 465.84, 459.24, 464.76, 459.09, 463.52, and 458.51 eV, respectively.³⁶ Thus, Ti₃C₂T_x nanosheets are chemically bonded with TiO₂ nanoparticles through the O_x-Ti-C bond. Regarding the P-T-T composite (Figure S2c1 to S2c6), besides the C-F,

C-O, C-C, C-Ti-O_x, and C-Ti subpeaks, a small subpeak of C-N is fitted at the binding energy of 284.97 eV in the C1s core-level spectrum. There is no change found in the XPS spectra of both F1s and O1s in comparison with that in the T-T composite. However, the N1s spectrum is found to be fitted into three subpeaks of N-H, N-C, and N-Ti at the binding energies of 401.62, 399.68, and 398.66 eV, respectively.³⁷ Besides the S-S bond of wool keratin, the S-Ti2p bond is detected. The S2p spectrum is fitted into four subpeaks of S-S2p_{1/2}, S-S2p_{3/2}, S-Ti2p_{1/2}, and S-Ti2p_{3/2} at the binding energies of 164.58, 163.48, 159.31, and 158.21 eV, respectively.³⁸ Accordingly, the Ti2p XPS spectrum is fitted into eight subpeaks of Ti2p_{1/2}-N/S, O_x-Ti2p_{1/2}-C, Ti2p_{1/2}-O, Ti2p_{1/2}-C, Ti2p_{3/2}-N/S, O_x-Ti2p_{3/2}-C, Ti2p_{3/2}-O, and Ti2p_{3/2}-C, corresponding to the binding energies of 466.12, 464.61, 463.50, 461.74, 460.12, 458.51, 458.45, and 456.70 eV, respectively. Hence, it is believed that Ti₃C₂T_x is chemically bonded with TiO₂ via the O_x-Ti-C bond, and that TiO₂ or Ti₃C₂T_x is grafted on wool flakes and bonded together via both N-Ti and S-Ti bonds. With respect to the CP-T-T composite (Figure S2d1 to S2d4), the C1s XPS spectrum is fitted into five subpeaks of C-O, C-N, C-C, C-Ti-O_x, and C-Ti at the binding energies of 288.39, 285.93, 284.81, 283.48, and 281.38 eV, respectively. The N1s XPS spectrum is fitted into three subpeaks of NO_x,³⁹ N-C, and N-Ti at the binding energies of 406.48, 400.19, and 395.24 eV, respectively. The O1s XPS spectrum is fitted into four subpeaks of O-C, O-Ti, O_x-Ti-C, and NO_x at the binding energies of 532.51, 530.69, 529.82, and 528.59 eV, respectively. The Ti2p XPS spectrum is fitted into eight subpeaks of Ti2p_{1/2}-N, O_x-Ti2p_{1/2}-C, Ti2p_{1/2}-O, Ti2p_{1/2}-C, Ti2p_{3/2}-N, O_x-Ti2p_{3/2}-C, Ti2p_{3/2}-O, and Ti2p_{3/2}-C, corresponding to the binding energies of 466.43, 465.20, 464.15, 463.11, 460.13, 459.24, 458.69, and 457.56 eV, respectively. Thus, it is concluded that Ti₃C₂T_x is chemically bonded with TiO₂ via the O_x-Ti-C bond and the N element originally from wool keratin is doped into Ti₃C₂T_x and TiO₂ through the N-Ti bond.

Electronic Energy Band Structures. The DRS spectra in Figure 4a indicate that the P-T-T composite reflects

more slightly UV rays and visible lights than the T-T composite in the 200-800 nm range, implying that the incorporation of wool flakes can reduce the light absorbing of T-T composite. Conversely, after calcination the light absorbing capability of the CP-T-T composite is enhanced to a certain degree probably because of the removal of wool keratins on the composite surface. Based on the Tauc's equation,⁴⁰ the optical band gaps of the T-T, P-T-T, and CP-T-T composites in Figure 4b are calculated to be 2.95, 2.89, and 2.61 eV, respectively. In comparison with the T-T composite, the narrowed band gap of the P-T-T composite is mainly ascribed to the co-doping of N and S elements of wool keratin with $Ti_3C_2T_x$ and TiO_2 . The band gap of the CP-T-T composite further decreases may be due to the N doping of wool keratin with $Ti_3C_2T_x$ and TiO_2 . The valence bands of the three composites are obtained from their UPS spectra (Figure 4c).⁴¹ By extrapolating the straight segment of UPS spectra to intersect with the x-axis at the high binding energy region, the cut-off energy ($E_{cut-off}$) edges are estimated to be 17.92, 17.45, and 17.57 eV for the T-T, P-T-T, and CP-T-T composites under vacuum condition, respectively. Because the Fermi energy (E_{Fermi}) is equal to zero under vacuum condition, according to the equation: $E_{\phi}=21.2-(E_{cut-off}-E_{Fermi})$, the work functions (E_{ϕ}) of the T-T, P-T-T, and CP-T-T composites are calculated to be 3.28, 3.75, and 3.63 eV under vacuum condition, respectively. Their corresponding valence band (E_{VBM}) edges are estimated to be 1.65, 1.82, and 1.84 eV by extrapolating the straight segment of UPS spectra to intersect with the x-axis at the low binding energy region under vacuum condition, respectively. As the E_{VBM} is lower than the E_{ϕ} under vacuum condition, thus the E_{VBM} edges of the T-T, P-T-T, and CP-T-T composites are calculated to be -4.93, -5.57, and -5.47 eV at the vacuum level, respectively. Based on the equation: E_{VBM} (normal hydrogen electrode, NHE) = -4.5 - E_{VBM} (vacuum level) eV, the E_{VBM} edges are determined to be 0.43, 1.07, and 0.97 eV for the T-T, P-T-T, and CP-T-T composites relative to the NHE, respectively. By considering the calculated band gaps, according to the equation: $E_{CBM}=E_{VBM}-E_g$, the conduction band (E_{CBM}) edges of the T-T, P-T-T, and CP-T-

T composites are calculated to be -2.52 , -1.82 , and -1.64 eV with respect to the NHE. The schematic of electronic energy bands in Figure 4d suggests that the photo-generated holes at valence band (VB) cannot oxidize OH^- or H_2O into $\cdot\text{OH}$ radicals (1.99 eV for $\cdot\text{OH}/\text{OH}^-$). However, the excited electrons at conduction band (CB) can reduce O_2 to $\cdot\text{O}_2$ (0.33 eV for $\text{O}_2/\cdot\text{O}_2^-$).⁴² Therefore, the photo-generated electrons might be the main reactive species. As compared with the P-T-T composite, more photogenerated electrons might be produced on the CP-T-T composite because of its narrowed band gap.

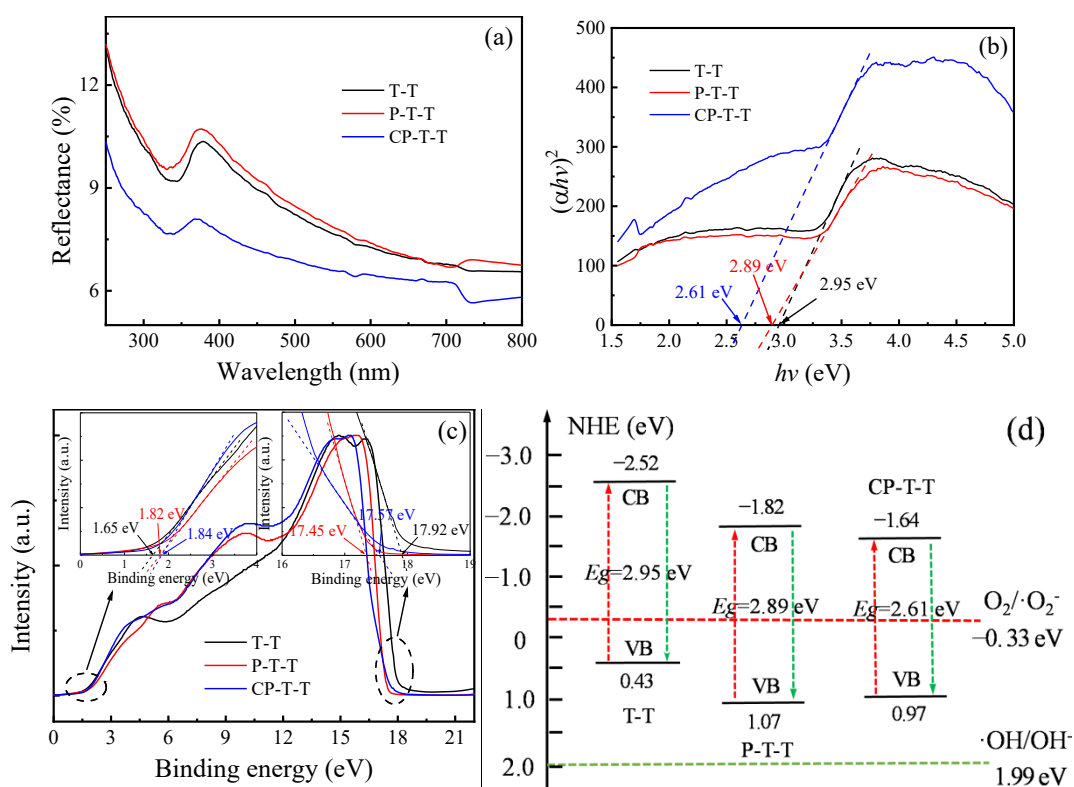


Figure 4. The (a) DRS spectra and (b) corresponding plots of $(\alpha hv)^2$ versus $h\nu$, the (c) UPS spectra inserted with the Fermi energy edges and cut-off edges, and the (d) schematic of electronic energy bands for the T-T, P-T-T and CP-T-T composites.

Photocatalysis Performance. The images of the color changes of the dye solutions at different irradiation time durations in Figure 5a and 5b indicate that the color changes of the blue dye solutions are different for the

two composites. Amazingly, as the irradiation time duration increases, the colors of the blue dye aqueous solutions degraded by the P-T-T composite gradually change from baby blue to light red. Nevertheless, the colors of the identical dye solutions degraded by the CP-T-T composite turn to colorless. The maximum absorption band at 602 nm is blue shifted for the P-T-T composite, while it is kept for the CP-T-T composite. This implies that different intermediate products are produced in the dye photodegradation process, which are probably caused by various active species generated from the composites. The UV absorption spectra in Figure S3a and S3b shows that the characteristic absorption band at 295 nm, which is assigned to the large aromatic ring system with electron-donating groups in the dye molecule,⁴³ decreases substantially and almost disappears with the increase of irradiation time duration for the CP-T-T. This suggests either the destruction of chromophore and conjugated system or its adsorption to the amino acids of wool keratin peptide. For the P-T-T composite, the absorption band at 295 nm is maintained, but at the same time a weak broad band at around 270 nm is observed, indicating some new compounds might be formed. The effects of the wool keratin peptides on the photocatalytic performance of the P-T-T composite are investigated by examining their E_A values and photodegradation curves of C.I. Reactive Blue 194 (Figure 5c and Figure S3c). Apparently, the mass ratio of wool flakes to $Ti_3C_2T_x$ nanosheets has great effects on the E_A and k values of the resultant composites. When the mass ratio of wool to $Ti_3C_2T_x$ reaches at 1:4, the resultant composite photocatalyst has a strong adsorption capability towards C.I. Reactive Blue 194 dye with the first and second E_A values of 95.3% and 46.9% as well as the highest k value of 0.053 min^{-1} . Accordingly, considering the adsorption capacity and photocatalytic behaviors, the mass ratio of wool to $Ti_3C_2T_x$ 1:4 is selected to prepare the P-T-T composite, which is further annealed in nitrogen environment to prepare the CP-T-T composite.

Figure S3d to S3f and Figure 5d to 5f show the photocatalytic behaviors of the T-T, P-T-T, and CP-T-T

composites toward C.I. Reactive Blue 194, TC-HCl, and LFX under visible light. The degradation curves of dye and antibiotics for all the three composites follow the pseudo-first-order reaction kinetics. Because the adsorption capacity and photocatalytic properties of photocatalysts are greatly influenced by its surface area, the k values of the three composites are calculated by considering their specific surface areas. Besides a superior quadratic adsorption capability towards the dyes, the P-T-T composite exhibits the highest k value of $5.4 \times 10^{-4} \text{ min}^{-1} \cdot \text{m}^{-2} \cdot \text{g}$, while the E_D values for all the three composites are similar and large than 98% (Figure 5d). This might be ascribed to various amino acid groups of wool keratins which is specifically affinity to organic dye molecules. With respect to TC-HCl, the E_D values for all the composites after 100 min of irradiations are beyond 70%, and the P-T-T composite behaves slightly better than the other two composites (Figure 5e). In the case of LFX, the adsorption and degradation capabilities of the CP-T-T composite are much better than the other two composites (Figure S3f and Figure 5f). Previous studies have reported that the peptide-modified TiO_2 can selectively and rapidly degrade streptavidin, but is greatly inhibited for the photocatalytic degradation of lysozyme.⁴⁴ The N-(9-fluorenylmethoxycarbonyl)-protected phenylalanine-phenyl-alanine-aspartic acid tripeptide can control the structure and photocatalytic activity of as-synthesized peptide- TiO_2 hybrid nanofibers via the calcination process.⁴⁵ In a summary, the P-T-T composite has the selective photocatalytic degradation properties toward different organic contaminants induced by calcination. In addition, after five successive measurements in Figure S3g to S3i, the E_D and E_A values toward TC-HCl for all the composites decrease with the increase of the number of cycles. The adsorption and photodegradation of TC-HCl follow the orders of T-T > P-T-T > CP-T-T from the points of reusability and stability.

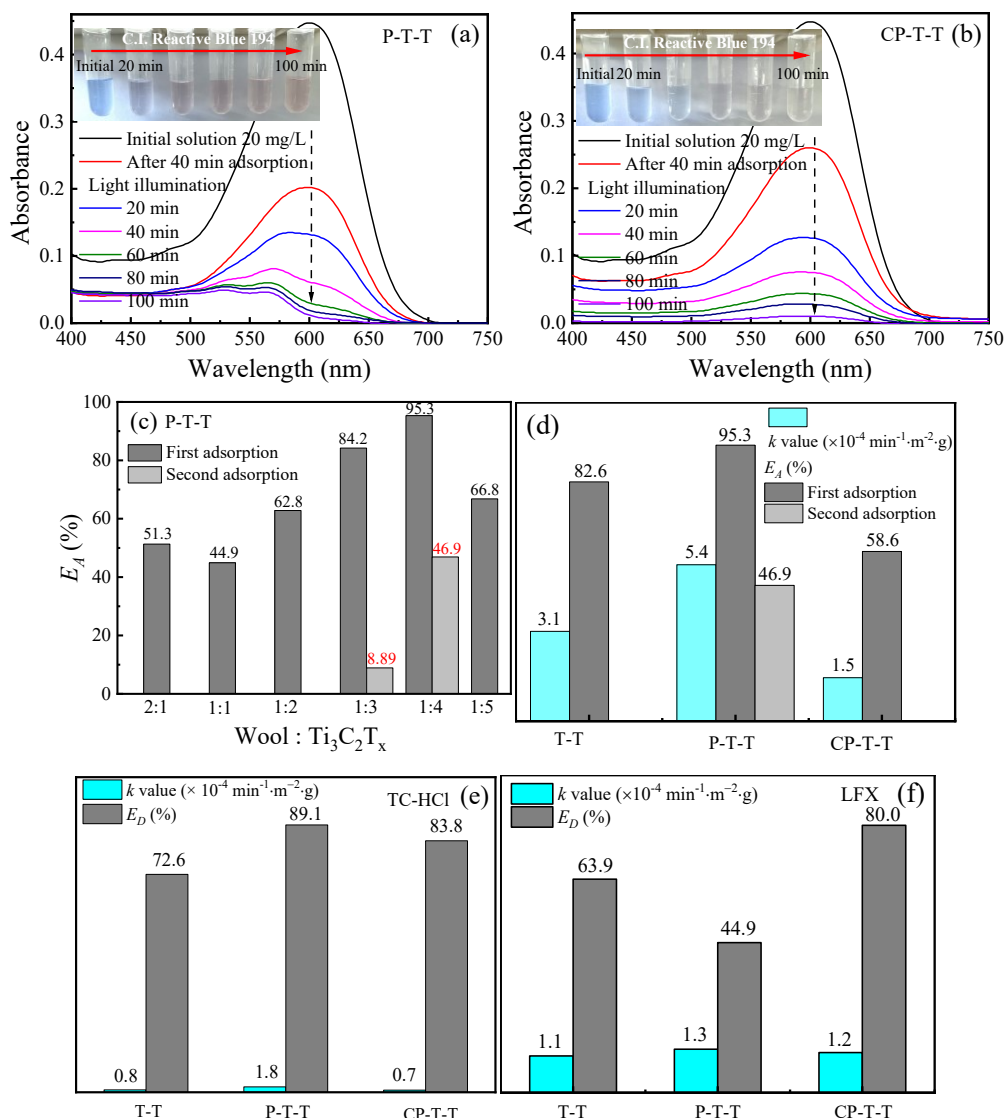


Figure 5. The time-dependent visible light absorbance spectra of C.I. Reactive Blue 194 dye solution by the (a) P-T-T and (b) CP-T-T composites; The (c) comparison of E_A values of C.I. Reactive Blue 194 by the P-T-T composites with different mass ratios of wool to $Ti_3C_2T_x$; The comparison of k and E_D (or E_A) values for the (d) C.I. Reactive Blue 194, (e) TC-HCl, and (f) LFX by the T-T, P-T-T, and CP-T-T composites, respectively.

Zeta Potentials and Separation Efficiencies of Photoinduced Electron-Hole Pairs. Figure 6a shows the zeta potential distribution curves of as-prepared composites in neutral aqueous solution. The mean zeta potential of the T-T composite is measured as -1.82 mV, which might be ascribed to the functional groups of OH^- and F^-

of $\text{Ti}_3\text{C}_2\text{T}_x$.⁴⁶ When wool flakes are incorporated with the T-T, the mean zeta potential of the P-T-T composite is reduced to -3.29 mV, implying more electro-negative groups are introduced by the wool keratins.⁴⁷ After calcination treatments, the mean zeta potential of the CP-T-T composite decreases further to -4.28 mV, suggesting that the carbonized wool keratin does not change its surface electronegativity. Thus, the surface potentials of the three composites have relatively little effect on the photocatalytic properties of the composites. Figures 6b to 6d show the steady-state PL emission spectra, EIS Nyquist plots, and transient photocurrent curves of the composites. It is believed that the smaller the intensity of the PL spectrum, the slower the recombination of photogenerated electron-hole pairs, resulting in the higher photocatalytic activity.⁴⁸ The PL intensity of the T-T composite is smaller than that of the P-T-T composite, but greater than that of the CP-T-T composite. Hence, the incorporation of wool flakes with T-T is thought to inhibit the separation of photogenerated electron-hole pairs, and the porous-structured CP-T-T composite is believed to help separation of photogenerated electrons and holes. In addition, the maximum PL emission peak is blue shifted because of the Burstein-Moss effect.⁴⁸ For the EIS plots, the arc radius of the T-T composite is smaller than that of the P-T-T, but larger than that of the CP-T-T. Apparently, the faster migration of photogenerated charges carriers occurs in the CP-T-T composite due to the lower charge transfer resistance. The transient photocurrent curves are in consistent with the EIS plots. The CP-T-T composite possesses the highest photocurrent, which behaves much better than the T-T composite. The P-T-T composite has the lowest photocurrent. Therefore, the conductive $\text{Ti}_3\text{C}_2\text{T}_x$ and the calcination process are beneficial to the separation and transfer of photogenerated charge carriers in the bulk materials and across their interfaces.

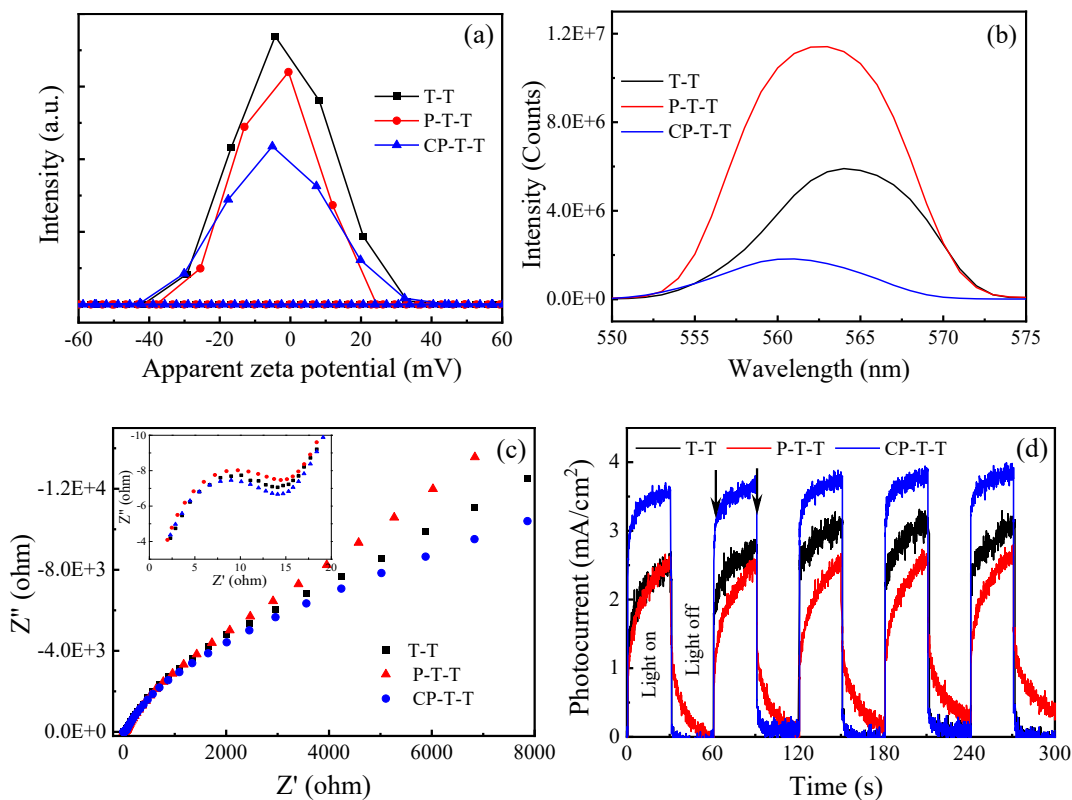
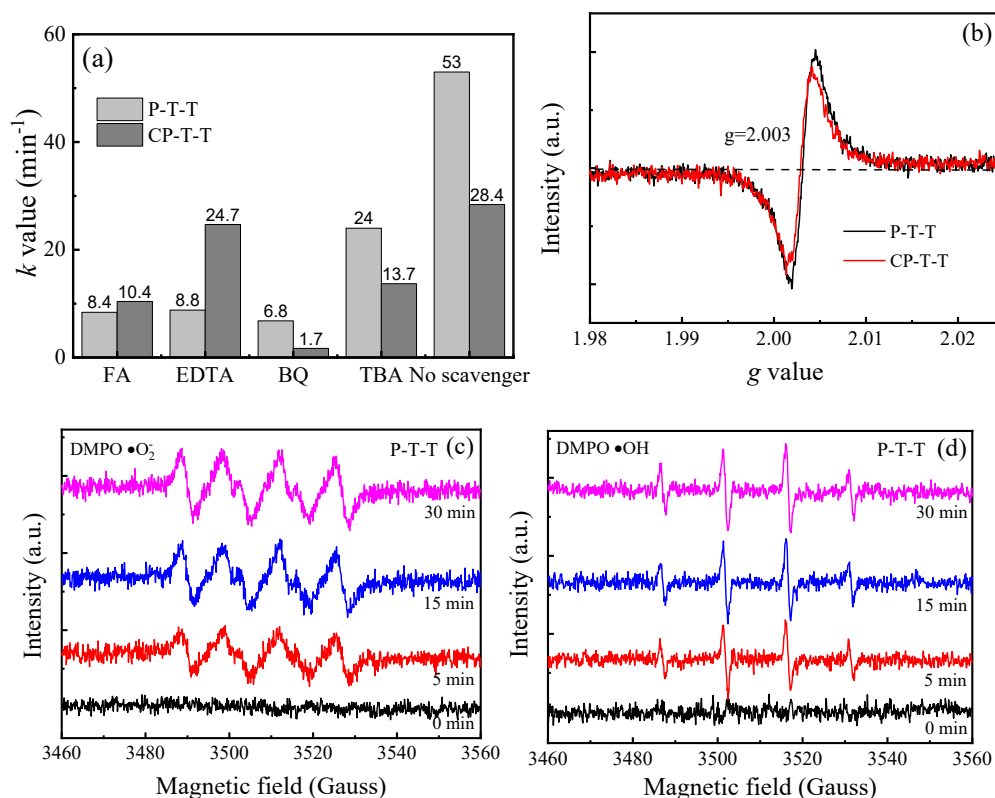


Figure 6. The (a) zeta potential distribution curves and (b) steady-state PL spectra, (c) EIS Nyquist plots, and (d) photocurrent curves for the T-T, P-T-T, and CP-T-T composites.

Determination of Reactive Species. After the scavengers of FA, EDTA, BQ and TBA are separately added into the dye solutions, the dye degradations are inhibited and the corresponding k values decrease to some degrees (Figure 7a, Figure S4a and S4b). The quench orders of reactive species are superoxide radicals ($\bullet\text{O}_2^-$) > singlet oxygen ($^1\text{O}_2$) > holes (h^+) > hydroxyl radicals ($\bullet\text{OH}$) for the P-T-T composite and $\bullet\text{O}_2^- > ^1\text{O}_2 > \bullet\text{OH} > h^+$ for the CP-T-T composite. Despite radicals $\bullet\text{O}_2^-$ and non-radicals $^1\text{O}_2$ are the dominant reactive species for both two composites, the reactive species generated in the two composites play different roles in the photodegradation process of C.I. Reactive Blue 194 dye with different colors. Furthermore, it is demonstrated that the main reactive species are $\bullet\text{O}_2^-$ and $\bullet\text{OH}$ for both $\text{TiO}_2/\text{Ti}_3\text{C}_2$ heterojunction⁴⁹ and $\text{In}_2\text{S}_3/\text{TiO}_2@\text{Ti}_3\text{C}_2\text{T}_x$ hybrid,⁴ $\bullet\text{O}_2^-$, e^- and h^+ for the $\text{TiO}_2/\text{Ti}_3\text{C}_2\text{T}_x$ heterojunction,²⁴ and $\bullet\text{O}_2^-$, $^1\text{O}_2$ and h^+ for the $\text{TiO}_2/\text{Ti}_3\text{C}_2\text{T}_x/\text{AgI}$ ternary composite.⁸

Consequently, the introduction of wool keratin has a small influence on the reactive species produced by T-T. As displayed in Figure 7b, the EPR signal at a g value of 2.003 is attributed to the trapped electrons by oxygen vacancy⁵⁰ in both composites. The intensity of oxygen vacancy for the P-T-T composite is slightly greater than that of the CP-T-T composite. This is probably derived from the reaction of holes with surface bridging oxygen atoms or lattice oxygen atoms.⁵¹ Additionally, the ESR spectra in Figure 7c to 7f validate the existence of $\bullet\text{O}_2^-$ and $\bullet\text{OH}$. Thus, the signal intensities of both $\text{DMPO}\text{-}\bullet\text{O}_2^-$ and $\text{DMPO}\text{-}\bullet\text{OH}$ increase gradually with the increase of irradiation time durations on both composites. After 30 min of visible light irradiation, the intensity of the CP-T-T composite is greater than that of the P-T-T composite (Figure S4c and S4d). Therefore, the active species are much more prone to produce in the CP-T-T composite than the P-T-T composite under visible light.



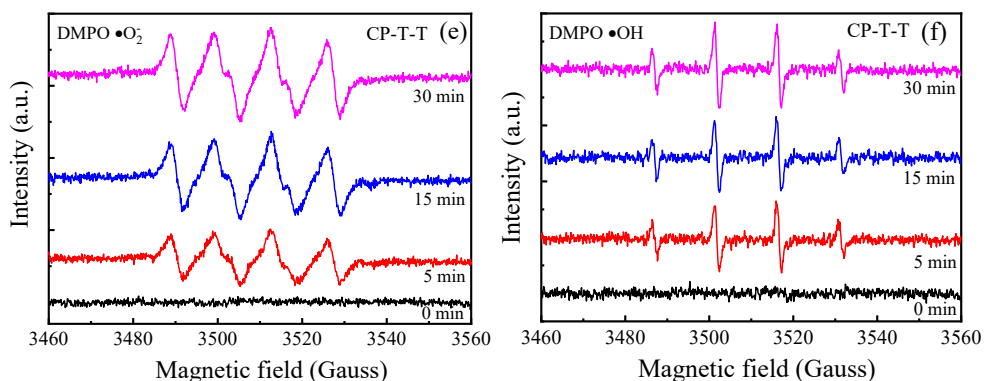


Figure 7. The (a) k values for the photodegradation of C.I. Reactive Blue 194 dye with different scavengers, (b) EPR spectra at 100 K, and ESR spectra of radical adducts trapped by DMPO for the detection of (c) and (e) $\bullet\text{O}_2^-$ in methanol dispersion, (d) and (f) $\bullet\text{OH}$ in aqueous dispersion for the P-T-T and CP-T-T composites, respectively.

Photodegradation Pathways. Figure S5 and Figure 8 show the possible proposed photodegradation pathways of C. I. reactive blue 194 by the P-T-T and CP-T-T composites. Figures S6 and S7 show the corresponding mass spectra of photodegradation intermediate products identified through MS measurement. The investigation is focused on the formation of major intermediate products to determine the probable degradation pathway. The deprotonated quasi-molecular ion peak at the mass-to-charge ratio (m/z) of 378.29624 indicates the presence of parent dye molecule with absence of three sodium ions $\text{C}_{33}\text{H}_{22}\text{ClN}_{10}\text{Na}_2\text{O}_{19}\text{S}_6^{3-}$. The dye degradation consists of three different pathways for both the composites because of the oxidation of active species. For the P-T-T composite (Figure S5), the main intermediates are probably substituted phenols which makes the solution light red.⁵² The first pathway starts with the cleavage of the N=N bond to generate $\text{C}_{16}\text{H}_{13}\text{N}_4\text{O}_{10}\text{S}_3^-$ at m/z 516.9979. The subtraction of sulfonate group results in the formation of $\text{C}_{16}\text{H}_{13}\text{N}_4\text{O}_8\text{S}_2^-$ at m/z 453.0180, which is oxidized to $\text{C}_{16}\text{H}_{10}\text{N}_3\text{O}_8\text{S}_2^-$ at m/z 435.9915, followed by the detachment of sulfonate group to produce $\text{C}_{16}\text{H}_{10}\text{N}_3\text{O}_6\text{S}^-$ at m/z 372.0296, and then the breakage of the N=N bond to generate $\text{C}_{10}\text{H}_5\text{O}_4$ at m/z 203.0219. Meanwhile, the N=N bond of $\text{C}_{16}\text{H}_{13}\text{N}_4\text{O}_{10}\text{S}_3^-$ is probably broken due to the radical attack, followed by the

successive subtraction of sulfonate groups to produce $C_{10}H_{10}N_3O_3^-$ at m/z 220.0728. The second pathway involves the cleavage of the N=N bond to form $C_{17}H_{14}ClN_5NaO_9S_3^-$ at m/z 585.9545, followed by the sulfonation to form $C_{17}H_{15}ClN_5O_9S_3^-$ at m/z 563.9726. After that, there exists two degradation sub-pathways. The first one is the subtraction of sulfonic acid to generate $C_{17}H_{13}ClN_5O_5S_2^-$ at m/z 466.0052, and then the breakage of the C-Cl bond via the hydroxylation to produce $C_{17}H_{14}N_5O_6S_2^-$ at m/z 448.0391. The second one involves the breakdown of the N=N bond followed by the hydroxylation to form $C_{17}H_{15}ClN_5O_{10}S_3^-$ at m/z 579.9675, and then to produce $C_{17}H_{13}ClN_5O_6S_2^-$ at m/z 482.0001, which is oxidized to form $C_{17}H_{13}ClN_5O_7S_2^-$ at m/z 497.9950, and sulfonyl group is further removed to produce $C_{15}H_{11}ClN_5O_5S^-$ at m/z 408.0175. The third pathway undergoes the cleavage of C-N bond linked benzene ring and triazine to form $C_{11}H_{11}ClN_5O_6S_2^-$ at m/z 407.9845 which is converted to $C_{11}H_{11}ClN_5O_2S^+$ at m/z 312.0316 or $C_{11}H_{13}ClN_5O_3S^+$ at m/z 330.0422 via the removal of sulfonyl group. The C-N bond is broken to generate $C_3H_4ClN_5$ at m/z 145.0155, followed by the cleavage of C-Cl bond to form $C_3H_5N_5$ at m/z 127.0794, and then the subtraction of hydroxylation of amino groups leads to the formation of $C_3H_3N_3O_3$ at m/z 129.0174. In the case of the CP-T-T composite (Figure 8), the reactive radicals preferentially attack the azo and amino groups of dye molecule. The first pathway proceeds via the cleavage of N=N bond to yield $C_{16}H_{13}N_4O_{10}S_3^-$ at m/z 516.9799, which is oxidized to $C_{10}H_{10}N_3O_7S_2^-$ at m/z 347.9965 owing to the breaking of N=N bond. This is followed by the elimination of sulfonate group to produce $C_{10}H_{10}N_3O_4S^-$ at m/z 268.0397, and subsequent formation of $C_8H_7N_2O_4^-$ at m/z 195.0411 due to the breaking of naphthalene ring, and the amino group is removed to form $C_8H_5O_4^-$ at m/z 165.0193. The second pathway involves the cleavage of N=N bond to produce $C_{17}H_{16}ClN_6O_9S_3^-$ at m/z 578.9835, followed by the oxidation hydroxylation of the resulting intermediates to yield $C_{17}H_{15}ClN_5O_{10}S_3^-$ at m/z 579.9675. The third pathway begins with the oxidative cleavage of N=N bond to form $C_{17}H_{15}ClN_5O_9S_3^-$ at m/z 563.9726, which is transformed to $C_{17}H_{13}ClN_5O_5S_2^-$ at m/z 466.0052 because of the

elimination of a sulfonic acid, and then converted into $C_9H_6ClN_4O_4S^-$ at m/z 300.9803 owing to the cleavage of C-N bond. Afterward two sub-pathways exist. The first one involves the cleavage of C-N bond to yield $C_6H_6NO_3S^-$ at m/z 172.0074, which is oxidized to $C_6H_6NO^-$ at m/z 108.0455 and further transformed to $C_6H_5O_2^-$ at m/z 109.0295. The second one undergoes the breakage of C-N bond to form $C_3H_2ClN_4O^-$ at m/z 144.9922, which is oxidized to $C_3H_3N_4O_2^-$ at m/z 127.0261. The resulting $C_{17}H_{15}ClN_5O_9S_3^-$ is probably oxidized to $C_{11}H_{11}ClN_5O_6S_2^-$ at m/z 407.9845, and then oxidized to $C_8H_{10}N_6S_2^-$ at m/z 279.9955. It is believed that all the intermediate products for both composites are degraded into small chain aliphatic acids, such as succinic acid, malonic acid, oxalic acid, dihydroxy acetic acid, acetic acid, formic acid, via various radical-initiated ring opening transformative and oxidative steps.⁵³ These products of smaller molecule weight are finally mineralized to H_2O , CO_3^{2-} , NO_3^- , Cl^- , SO_4^{2-} , and NH_4^+ .

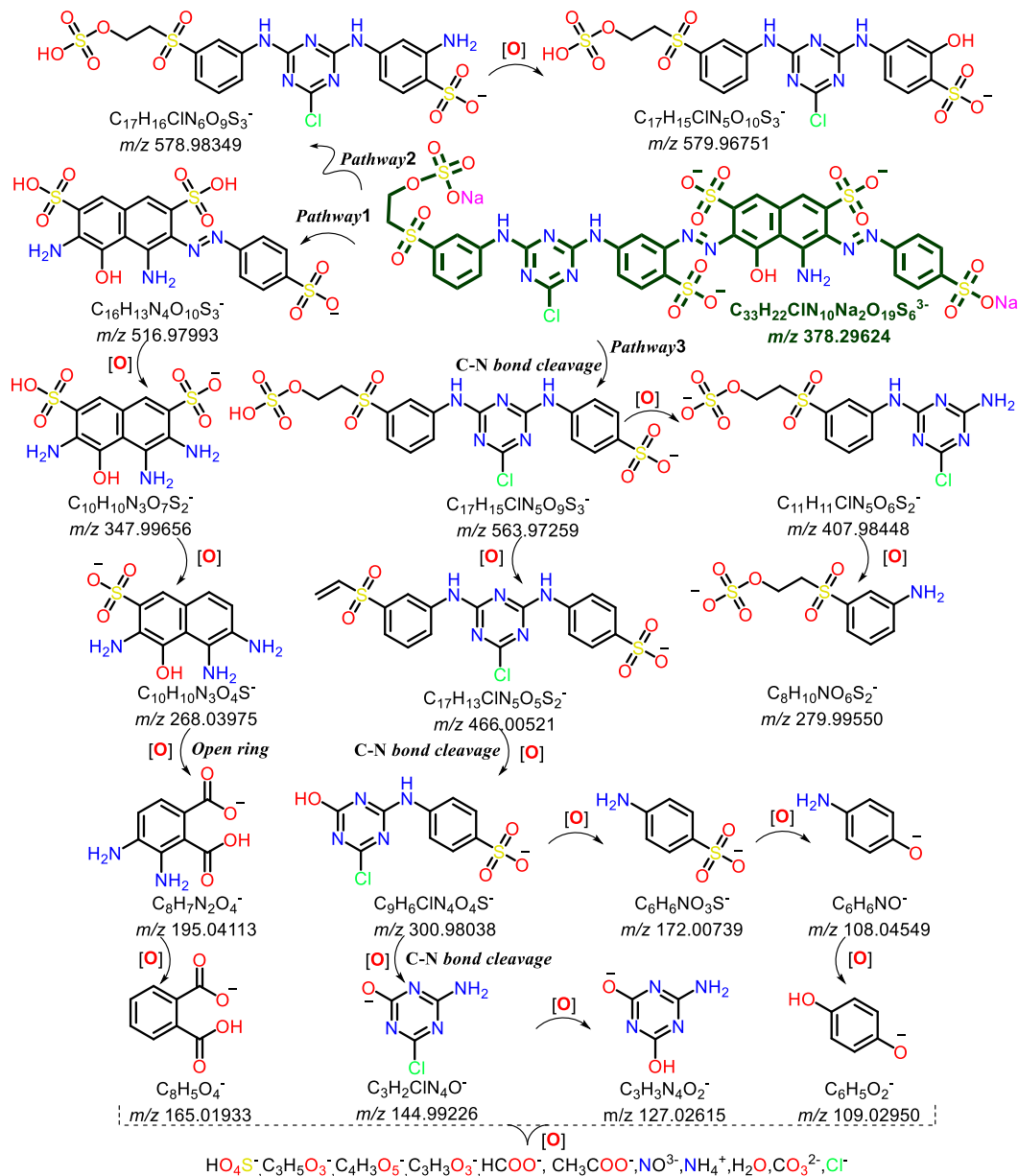


Figure 8. The possible photodegradation pathways of C.I. Reactive Blue 194 dye by the CP-T-T composite under visible light.

Amino Acid Compositions and Organic Elements. Figure S8 and Table S2 show the gas chromatograms and the quantitative amino acid composition data of wool fiber, P-T-T and CP-T-T composites, respectively. It is known that the wool keratin is composed of seventeen different amino acids, and the top five amino acids in content are glutamic acid, proline, arginine, leucine and serine.²⁸ Although the cystine content of wool keratin is

affected by hydrochloric acid used for the hydrolysis of wool fibers,⁵⁴ the contents of other amino acids are in accordance with previous studies.²⁸ For the P-T-T composite, seventeen amino acids are remained, but the amount of each is significantly reduced in comparison with them in original wool fibers. The top five amino acids in content are isoleucine, methionine, arginine, proline and leucine. It means that these amino acids could be probably partially disrupted or dissolved under high-temperature and high-pressure condition in the presence of chemical agents. Amazingly, after calcination these seventeen amino acids are still maintained, but the amount of each amino acid in the CP-T-T composite decreases to different levels. The top five amino acids in content are isoleucine, methionine, valine, cystine and leucine probably due to their superior thermal stabilities.⁵⁴ Another important reason is perhaps because the wool flakes are sandwiched between $Ti_3C_2T_x$ nanosheets to form a compacted hybrid, which is covered by a layer of TiO_2 nanoparticles. Thus a few of wool keratin inside the resultant composite are kept despite most of amino acids of wool keratin are lost. Those exposed wool keratin on composite surface should be carbonized to form a N-doped carbon coating. As displayed in Figure S9, the TGA curve confirms that the organic components of the P-T-T composite decrease with the increase of heating temperature, and a few substances (2%) are remained at 400 °C in nitrogen gas atmosphere. The changes of amino acid components suggest that seventeen amino acids are subjected to different breakages in the hydrothermal and/or calcination procedures, which might produce a series of polypeptides⁵⁴ grafted with $Ti_3C_2T_x$ or TiO_2 . In addition, the organic elements of P-T-T and CP-T-T composites are analyzed, and Table S3 shows the analysis results. The contents of C, H, N, S and O elements are reduced from 4.690%, 1.345%, 0.880%, 0.208%, and 7.586% to 5.255%, 0.647%, 0.300%, 0.114%, and 4.790% when the P-T-T composite is calcined at nitrogen atmosphere. The reduction of organic elements in the composite might facilitate the separation of photo-induced charge carriers.

The First Principles Calculations. Figure 9 shows the atomic structure diagrams and corresponding partial density of states, and the charge density differences of the T-T and P-T-T composites. The atomic models in Figure 9a indicate that the optimized lattice constants of $\text{Ti}_3\text{C}_2\text{T}_x$ and TiO_2 are calculated to be 3.071 and 3.793 Å respectively, which are highly consistent with previous studies.^{55,56} As displayed in Figure 9b, the partial density of states (PDOS) suggest the metallic characteristics of both T-T and P-T-T composites with no magnetism. There exist several discontinuous states in the energy region between -2.8 and -0.5 eV for the T-T composite. When the wool keratins (amino acid peptide chains) are incorporated with $\text{Ti}_3\text{C}_2\text{T}_x$ and TiO_2 complex, the PDOS becomes continuous in the energy range from -2.8 and -1.8 eV. Meanwhile, a new state is noticed in the energy range of -0.65 to -0.6 eV in the PDOS, which is mainly derived from the S orbital of peptide. The charge density differences in Figure 9c imply that the electron accumulation and depletion appear on TiO_2 and $\text{Ti}_3\text{C}_2\text{T}_x$ in the T-T composite, individually. Nevertheless, for the P-T-T composite, the introduction of peptide chains changes the interaction between TiO_2 and $\text{Ti}_3\text{C}_2\text{T}_x$, resulting in the redistribution of the electrons accumulation and depletion. Moreover, the bond strength between peptide and $\text{Ti}_3\text{C}_2\text{T}_x$ is relatively greater than that between peptide and TiO_2 .

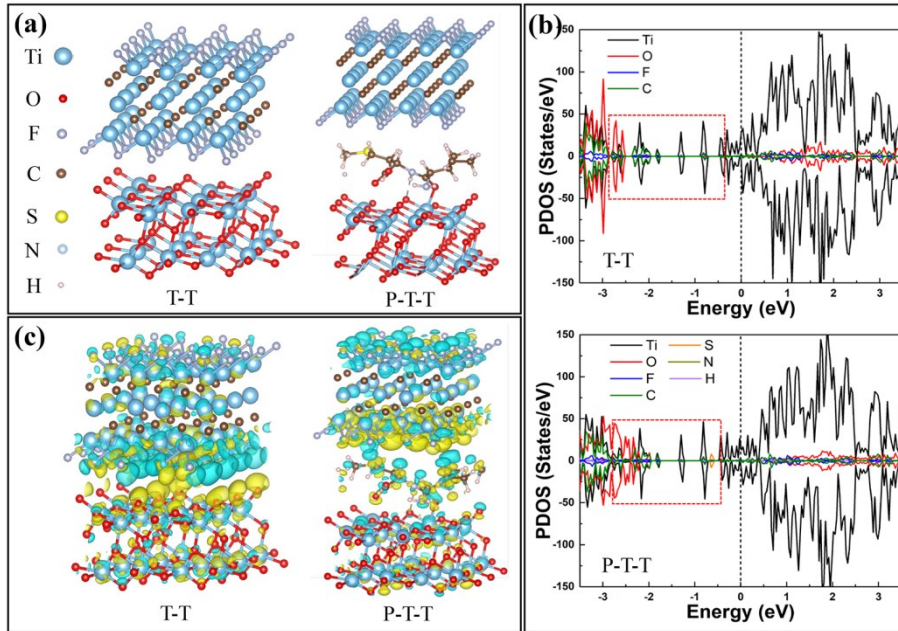


Figure 9. The (a) atomic structure diagrams and (b) corresponding partial density of states and the (c) charge density differences of T-T and P-T-T composites, respectively. Note: the electron depletion and accumulation regions are separately marked with cyan and yellow colors.

Reaction Mechanism Analysis. As a summary of the analysis above, we deduced the reaction mechanism diagrams of the T-T, P-T-T, and CP-T-T composites, as displayed in Figure 10. For the T-T heterojunction (Figure 10a), the photogenerated electrons at the interface of Ti₃C₂T_x and TiO₂ migrate from Ti₃C₂T_x to TiO₂ across the Schottky contact, thus an internal electron field is constructed. The direction of the IEF is from Ti₃C₂T_x to TiO₂. The photogenerated electrons produced from TiO₂ will transfer to Ti₃C₂T_x driven by the IEF.¹² In the P-T-T composite, the peptide chains of wool keratins are introduced between Ti₃C₂T_x and TiO₂, the original IEF is destroyed and a new IEF is formed at the interface of peptide chains and Ti₃C₂T_x as demonstrated by DFT calculations. The direction of the IEF points towards Ti₃C₂T_x from peptide chains (Figure 10b). Thus, it is difficult for the photogenerated electrons produced by TiO₂ to shift to Ti₃C₂T_x across the peptide chains because of the unfavorable IEF, the poor conductivity of wool keratin, and the increased distance between TiO₂ and Ti₃C₂T_x.

Nevertheless, the photogenerated holes produced from TiO_2 are relatively prone to move to peptide chains, and thereby the IEF is probably strengthened. These photogenerated holes could move through the strengthened internal electric field and trapped in the composite. The photogenerated electrons accumulated on the surface of N and S co-doped TiO_2 (as confirmed by XPS) react with the dissolved oxygen to produce $\bullet\text{O}_2^-$ radicals, followed by the formation of $\bullet\text{OH}$ radicals which can degrade the adsorbed dye molecules. By considering its energy band structure, the photo-generated holes react with $\bullet\text{O}_2^-$ radicals to produce $^1\text{O}_2$ radicals which degrade dye molecules. Additionally, the peptide chains of wool keratins facilitate the selective chemical adsorption of dye molecules due to the carboxyl and amino groups of peptides, resulting in the intimate contact of dye molecules with the composite. Therefore, the photocatalytic activity of the P-T-T composite is dominated by the chemical adsorption enhancement, and thus a highly efficient photocatalytic performance toward organic dyes is obtained despite the transfer of photoinduced charge carriers is inhibited to some degree. After calcination in nitrogen environment, the exposed peptide chains of wool keratin on/near the surface of the CP-T-T composite are carbonized with the loss of F and S elements, resulting in a good electrical conductivity. It has been proved that the hydrophobic features can be obtained when the keratin- TiO_2 composite is calcined and many meso- and micro-pores are formed, exhibiting higher photodegradation efficiency to organic pollutants than the pure calcinated TiO_2 because of its special porous structure, large water contact angle, and high adsorption energy.⁵⁷ Moreover, more nanopores are produced as confirmed by BET results, which are favorable for the physical absorption toward dye molecules. Consequently, the outer component of the composite is mainly composed of the N-doped TiO_2 along with active N-doped carbon, and the internal component is primarily consisting of $\text{Ti}_3\text{C}_2\text{T}_x$ nanosheets and peptide chains of wool keratin combined with some TiO_2 nanoparticles to form the ternary heterojunction based on the preparation procedure employed. As verified by the results of amino acid compositions and organic elements, most of wool

keratin are lost and a few peptide chains of wool keratin are remained inside the composite, which results in the enhanced IEF owing to the reduction of interface distance between TiO_2 and $\text{Ti}_3\text{C}_2\text{T}_x$ (Figure 10c). In this case, the photogenerated electrons produced by TiO_2 would easily transfer to $\text{Ti}_3\text{C}_2\text{T}_x$ across the reduced peptide chains of wool keratin, meanwhile, the N and S elements of peptide are likely to dope with TiO_2 and $\text{Ti}_3\text{C}_2\text{T}_x$. Therefore, the photocatalytic activity of the CP-T-T composite is predominated by the electron transfer enhancement. It is concluded that the degradation pathways of C.I. Reactive Blue 194 dye in the P-T-T composite are dominated by the enhancement of selective chemical adsorptions and that in the CP-T-T composite are determined by both the physical adsorption of the resultant N-doped TiO_2 contaminated with active carbon and the improved electron transfer across the decreased peptide chains. The above analysis reveals that the incorporation of the peptide chains of wool keratin between $\text{Ti}_3\text{C}_2\text{T}_x$ and TiO_2 leads to the redistribution of the electron accumulation and depletion among peptide, $\text{Ti}_3\text{C}_2\text{T}_x$ and TiO_2 , which changes the IEF. The calcination at nitrogen atmosphere results in two changes in the resultant composite. One is the formation of electrically conductive active carbon layer on composite surface, which changes the adsorption capability and electron conduction pathways of the composite towards organic dye. Another is the enhanced IEF which is beneficial for the separation and transfer of photogenerated electron-electron pairs. So, the calcination leads to the transformation from the adsorption-mediated photocatalytic degradation of organic dye by the P-T-T composite to the charge transfer-mediated photocatalytic degradation of the same dye by the CP-T-T composite.

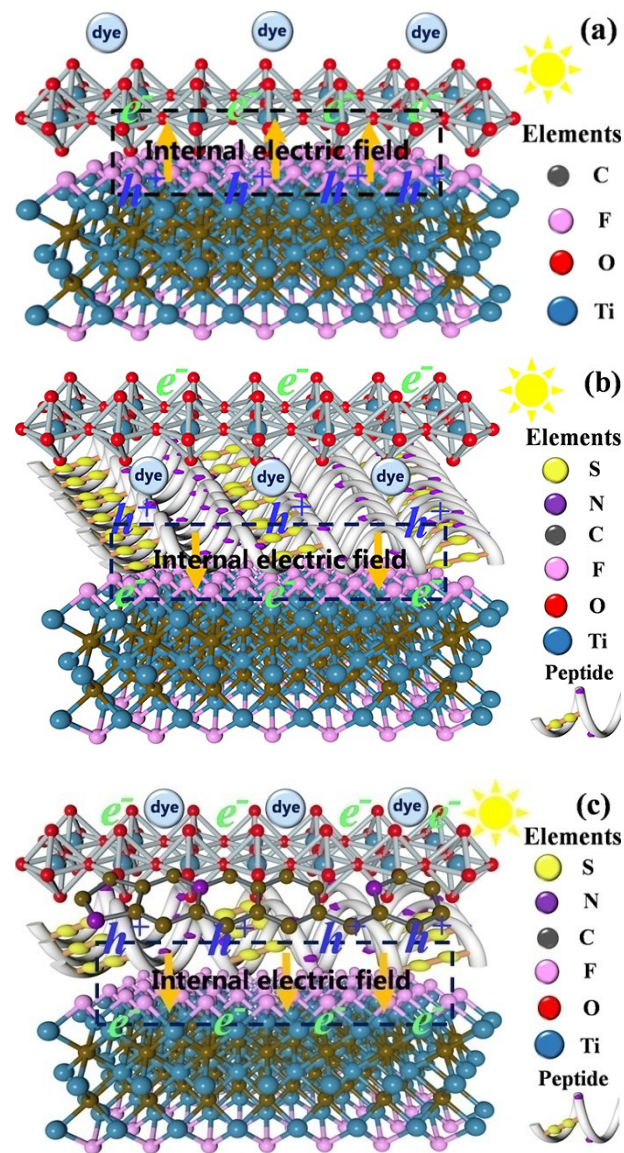


Figure 10. The reaction mechanism diagrams of a unit cell model of the (a) T-T, (b) P-T-T, and CP-T-T composites for the photocatalytic degradation of organic dye.

CONCLUSIONS

In brief, the structure characterizations indicated that the BET specific surface area of the T-T composite was reduced from 140.4 to 97.3 m²/g when the peptide chains of wool keratin was introduced, but increased to 190.9 m²/g after calcination in nitrogen gas. The micropores and mesopores of the CP-T-T composite provided more active sites for the photodegradation of adsorbed organic pollutants. The intimate contacts among peptide,

$\text{Ti}_3\text{C}_2\text{T}_x$ and TiO_2 were beneficial for the transfer and separation of charge carriers. $\text{Ti}_3\text{C}_2\text{T}_x$ and TiO_2 were chemically grafted with peptide chains of wool keratin through the bonds of $\text{O}_x\text{-Ti-C}$, N-Ti and S-Ti . Compared with the T-T composite, the band gap of the P-T-T composite was reduced and further decreased after calcination. The photocatalytic degradations of C.I. Reactive Blue 194, TC-HCl and LFX validated that the P-T-T composite exhibited different photocatalytic activities towards various organic pollutants. The selective photocatalytic property of the P-T-T composite was gained via the calcination process. The calcination process in nitrogen environment was helpful for the separation and transfer of photogenerated charge carriers in the CP-T-T composite. The photodegradation pathways of C.I. Reactive Blue 194 dye were different for the P-T-T and CP-T-T composites. The first principles calculations demonstrated that the incorporation of peptide chains of wool keratin with T-T led to the redistribution of the electron accumulation and depletion on peptide, $\text{Ti}_3\text{C}_2\text{T}_x$ and TiO_2 , which changed the direction of IEF in the composite. Importantly, the adsorption-mediated photocatalytic degradation of C.I. Reactive Blue 194 dye by the P-T-T composite was transformed to the charge transfer-mediated photocatalytic degradation of the same dye by the CP-T-T composite.

ASSOCIATED CONTENT

Supporting Information

The Supporting Information is available free of charge at the ACS website.

Additional data on materials and reagents, preparations of wool flakes and few-layered $\text{Ti}_3\text{C}_2\text{T}_x$ nanosheets, characterization techniques, purification of dyes, analysis of photodegradation products, FESEM images, AFM results, XPS survey and core-level spectra, XPS elemental analysis results, photodegradation curves, trapping experiments, ESR spectra, possible photodegradation pathways of C.I. Reactive Blue 194 dye, mass spectra, gas

chromatograms, amino acid compositions, TGA curve, organic elements of the as-prepared composites, and first principles calculations.

AUTHOR INFORMATION

Corresponding Authors

Hui Zhang - *School of Textile Science & Engineering, Xi'an Polytechnic University, Xi'an, Shaanxi 710048, PR China*; orcid.org/0000-0001-6305-8670; Email: hzhangw532@xpu.edu.cn

Ningtao Mao - *School of Design, University of Leeds, Leeds, LS2 9JT, United Kingdom*; Email: n.mao@leeds.ac.uk

Authors

Jiale Yao - *School of Textile Science & Engineering, Xi'an Polytechnic University, Xi'an, Shaanxi 710048, PR China*

Xinyue Zhang - *School of Environmental and Chemical Engineering, Xi'an Polytechnic University, Xi'an, Shaanxi 710048, PR China*

Chengyu Fu - *School of Textile Science & Engineering, Xi'an Polytechnic University, Xi'an, Shaanxi 710048, PR China*

Yaping Miao - *School of Textile Science & Engineering, Xi'an Polytechnic University, Xi'an, Shaanxi 710048, PR China*

Yani Guo - *School of Environmental and Chemical Engineering, Xi'an Polytechnic University, Xi'an, Shaanxi 710048, PR China*

Zhi Tong - *School of Environmental and Chemical Engineering, Xi'an Polytechnic University, Xi'an, Shaanxi*

Notes

The authors declare no competing financial interest.

ACKNOWLEDGMENTS

This study was supported by the National Natural Science Foundation of China (No. 51873169 and No. 52202111), the Research Project of General Administration of Customs Peoples Republic of China (No. 2020HK261), and the Key Research and Development Projects of Shaanxi Province (No. 2022GY-191).

REFERENCES

- (1) Lim, K. R. G.; Handoko, A. D.; Nemani, S. K.; Wyatt, B.; Jiang, H. Y.; Tang, J. W.; Anasori, B.; She, Z. W. Rational Design of Two-Dimensional Transition Metal Carbide/Nitride (MXene) Hybrids and Nanocomposites for Catalytic Energy Storage and Conversion. *ACS Nano* **2020**, *14*, 10834–10864.
- (2) Zhong, Q.; Li, Y.; Zhang, G. K. Two-Dimensional MXene-Based and MXene-Derived Photocatalysts: Recent Developments and Perspectives. *Chem. Eng. J.* **2021**, *409*, 128099.
- (3) Wang, H.; Wu, Y.; Xiao, T.; Yuan, X. Z.; Zeng, G. M.; Tu, W. G.; Wu, S. Y.; Lee, H. Y.; Tan, Y. Z.; Chew, J. W. Formation of Quasi-Core-Shell In₂S₃/Anatase TiO₂@Metallic Ti₃C₂T_x Hybrids with Favorable Charge Transfer Channels for Excellent Visible-Light-Photocatalytic Performance. *Appl. Catal. B-Environ.* **2018**, *233*, 213–225.
- (4) Ai, Z. Z.; Zhang, K.; Xu, L. L.; Huang, M. L.; Shi, D.; Shao, Y. L.; Shen, J. X.; Wu, Y. Z.; Hao, X. P. In Situ

Configuration of Dual S-Scheme BP/(Ti₃C₂T_x@TiO₂) Heterojunction for Broad Band Spectrum Solar-Driven Photocatalytic H₂ Evolution in Pure Water. *J. Colloid. Interf. Sci.* **2022**, *610*, 13–23.

- (5) Yang, L. F.; Chen, J.; Que, M. D.; Liu, X. W.; Zheng, H. Q.; Yang, T.; Liu, Z. K.; Li, Y. J.; Ma, Y. Z.; Yang, X. F.; et al. Construction of 2D/2D/2D BiOBr/(001)-TiO₂/Ti₃C₂T_x Heterojunction for Enhancing Photocatalytic Degradation of Dye. *J. Alloy. Compd.* **2022**, *893*, 162289.
- (6) Wu, J. L.; Zhang, Y.; Lu, P.; Fang, G. Q.; Li, X.; Yu, W. W.; Zhang, Z. Y.; Dong, B. Engineering 2D Multi-Hetero-Interface in the Well-Designed Nanosheet Composite Photocatalyst with Broad Electron-Transfer Channels for Highly-Efficient Solar-to-Fuels Conversion. *Appl. Catal. B-Environ.* **2021**, *286*, 119944.
- (7) Xu, T. X.; Wang, J. P.; Cong, Y.; Jiang, S.; Zhang, Q.; Zhu, H.; Li, Y. J.; Li, X. K. Ternary BiOBr/TiO₂/Ti₃C₂T_x MXene Nanocomposites with Heterojunction Structure and Improved Photocatalysis Performance. *Chinese Chem. Lett.* **2020**, *31*, 1022–1025.
- (8) Wu, F. D.; Chen, J. C.; Hu, J. P. Synthesis of TiO₂/Ti₃C₂T_x/AgI Z-Scheme Photocatalyst for Tetracycline Hydrochloride Photocatalytic Degradation. *J. Environ. Chem. Eng.* **2022**, *10*, 107117.
- (9) Lu, S. Y.; Meng, G.; Wang, C.; Chen, H. Photocatalytic Inactivation of Airborne Bacteria in a Polyurethane Foam Reactor Loaded with a Hybrid of MXene and Anatase TiO₂ Exposing {001} Facets. *Chem. Eng. J.* **2021**, *404*, 126526.
- (10) Zhou, Y. L.; Chai, Y. C.; Li, X. Y.; Wu, Z. H.; Lin, J.; Han, Y. J.; Li, L.; Qi, H. F.; Gu, Y. M.; Kang, L. L.; et al. Defect-Rich TiO₂ In Situ Evolved from MXene for the Enhanced Oxidative Dehydrogenation of Ethane to Ethylene. *ACS Catal.* **2021**, *11*, 15223–15233.
- (11) Rosales, M.; Garcia, A.; Fuenzalida, V. M.; Espinoza-Gonzalez, R.; Song, G. C.; Wang, B.; Yu, J. H.; Garcia, F.; Rosenkranz, A. Unprecedented Arsenic Photo-Oxidation Behavior of Few- and Multi-Layer Ti₃C₂T_x

- Nano-Sheets. *Appl. Mater. Today* **2020**, *20*, 100769.
- (12) Zhang, P.; Li, Y. K.; Zhang, Y. S.; Hou, R. H.; Zhang, X. L.; Xue, C.; Wang, S. B.; Zhu, B. C.; Li, N.; Shao, G. S. Photogenerated Electron Transfer Process in Heterojunctions: In Situ Irradiation XPS. *Small Methods* **2020**, *4*, 2000214.
- (13) Zong, S.; Liu, J. C.; Huang, Z. L.; Liu, L. L.; Liu, J. R.; Zheng, J.; Fang, Y. X. Mxene-TiO₂ Composite with Exposed {101} Facets for the Improved Photocatalytic Hydrogen Evolution Activity. *J. Alloy. Compd.* **2022**, *896*, 163039.
- (14) Debow, S.; Zhang, T.; Liu, X. S.; Song, F. Z.; Qian, Y. Q.; Han, J.; Maleski, K.; Zander, Z. B.; Creasy, W. R.; Kuhn, D. L.; et al. Charge Dynamics in TiO₂/MXene Composites. *J. Phys. Chem. C* **2021**, *125*, 10473–10482.
- (15) Tung, W. S.; Daoud, W. A. Photocatalytic Self-Cleaning Keratins: A Feasibility Study. *Acta Biomater.* **2009**, *5*, 50–56.
- (16) Zhang, H.; Yang, Z. W.; Zhang, X. T.; Mao, N. T. Photocatalytic Effects of Wool Fibers Modified with Solely TiO₂ Nanoparticles and N-Doped TiO₂ Nanoparticles by Using Hydrothermal Method. *Chem. Eng. J.* **2014**, *254*, 106–114.
- (17) Tran, T. H.; Nosaka, A. Y.; Nosaka, Y. Adsorption and Photocatalytic Decomposition of Amino Acids in TiO₂ Photocatalytic Systems. *J. Phys. Chem. B* **2006**, *110*, 25525–25531.
- (18) Zangeneh, H.; Mousavi, S. A.; Eskandari, P. Comparison the Visible Photocatalytic Activity and Kinetic Performance of Amino Acids (Non-Metal Doped) TiO₂ for Degradation of Colored Wastewater Effluent. *Mat. Sci. Semicon. Proc.* **2022**, *140*, 106383.
- (19) Lim, J.; Kwak, D. Y.; Sieland, F.; Kim, C.; Bahnemann, D. W.; Choi, W. Visible Light-Induced Catalytic

- Activation of Peroxymonosulfate Using Heterogeneous Surface Complexes of Amino Acids on TiO₂. *Appl. Catal. B-Environ.* **2018**, *225*, 406–414.
- (20) Hosseini, F.; Mohebbi, S. High Efficient Photocatalytic Reduction of Aqueous Zn²⁺, Pb²⁺ and Cu²⁺ Ions Using Modified Titanium Dioxide Nanoparticles with Amino Acids. *J. Ind. Eng. Chem.* **2020**, *85*, 190–195.
- (21) Bakre, P. V.; Tilve, S. G.; Ghosh, N. N. Investigation of Amino Acids as Templates for the Sol-Gel Synthesis of Mesoporous Nano TiO₂ for Photocatalysis. *Monatsh. Chem.* **2018**, *149*, 11–18.
- (22) Shkrob, I. A.; Chemerisov, S. D. Light Induced Fragmentation of Polyfunctional Carboxylated Compounds on Hydrated Metal Oxide Particles: from Simple Organic Acids to Peptides. *J. Phys. Chem. C* **2019**, *113*, 17138–17150.
- (23) Pan, Y. X.; Cong, H. P.; Men, Y. L.; Xin, S.; Sun, Z. Q.; Liu, C. J.; Yu, S. H. Peptide Self-Assembled Biofilm with Unique Electron Transfer Flexibility for Highly Efficient Visible-Light-Driven Photocatalysis. *ACS Nano* **2015**, *9*, 11258–11265.
- (24) Guo, L. Q.; Hu, Y. W.; Yu, B.; Davis, E.; Irvin, R.; Yan, X. G.; Li, D. Y. Incorporating TiO₂ Nanotubes with a Peptide of D-Amino K122-4 (D) for Enhanced Mechanical and Photocatalytic Properties. *Sci. Rep-UK* **2016**, *6*, 22247.
- (25) Li, K. N.; Zhang, S. S.; Li, Y. H.; Fan, J. J.; Lv, K. L. MXenes as Noble-Metal-Alternative Co-Catalysts in Photocatalysis. *Chinese J. Catal.* **2021**, *42*, 3–14.
- (26) Zeng, H.; Li, Z. H.; Li, G. S.; Cui, X. Q.; Jin, M. X.; Xie, T. F.; Liu, L. L.; Jiang, M. P.; Zhong, X.; Zhang, Y. W.; et al. Interfacial Engineering of TiO₂/Ti₃C₂MXene/Carbon Nitride Hybrids Boosting Charge Transfer for Efficient Photocatalytic Hydrogen Evolution. *Adv. Energy Mater.* **2022**, *12*, 2102765.
- (27) Fang, H. J.; Pan, Y. S.; Yin, M. Y.; Pan, C. L. Enhanced Photocatalytic Activity and Mechanism of Ti₃C₂-

- OH/Bi₂WO₆:Yb³⁺, Tm³⁺ Towards Degradation of RhB Under Visible and Near Infrared Light Irradiation. *Mater. Res. Bull.* **2020**, *121*, 110618.
- (28) Li, B.; Yao, J. B.; Niu, J. R.; Liu, J. Y.; Wang, L.; Feng, M.; Sun, Y. L. Study on the Effect of Organic Phosphonic Compounds on Disulfide Bonds in Wool. *Text. Res. J.* **2019**, *89*, 2682–2693.
- (29) Malakootian, M.; Nasiri, A.; Gharaghani, M. A. Photocatalytic Degradation of Ciprofloxacin Antibiotic by TiO₂ Nanoparticles Immobilized on a Glass Plate. *Chem. Eng. Commun.* **2020**, *207*, 56–72.
- (30) Liu, N.; Zheng, Y. J.; Jing, C. W.; Gao, B.; Huang, W. Y.; Li, Z. M.; Lei, J. Q.; Zhang, X. D.; Cui, L. F.; Tang, L. Boosting Catalytic Degradation Efficiency by Incorporation of MIL-53(Fe) with Ti₃C₂T_x Nanosheets. *J. Mol. Liq.* **2020**, *311*, 113201.
- (31) Kuang, D. L.; Wang, L.; Guo, X. Z.; She, Y.; Du, B. S.; Liang, C. Y.; Qu, W. J.; Sun, X.; Wu, Z. L.; Hu, W.; et al. Facile Hydrothermal Synthesis of Ti₃C₂T_x-TiO₂ Nanocomposites for Gaseous Volatile Organic Compounds Detection at Room Temperature. *J. Hazard. Mater.* **2021**, *416*, 126171.
- (32) Wang, C. J.; Shen, J.; Chen, R. G.; Cao, F.; Jin, B. Self-Assembled BiOCl/Ti₃C₂T_x Composites with Efficient Photo-Induced Charge Separation Activity for Photocatalytic Degradation of P-Nitrophenol. *Appl. Surf. Sci.* **2020**, *519*, 146175.
- (33) Su, T. M.; Hood, Z. D.; Naguib, M.; Bai, L.; Luo, S.; Rouleau, C. M.; Ivanoy, I. N.; Ji, H. B.; Qin, Z. Z.; Wu, Z. L. Monolayer Ti₃C₂T_x as an Effective Co-Catalyst for Enhanced Photocatalytic Hydrogen Production over TiO₂. *ACS Appl. Energ. Mater.* **2019**, *2*, 4640–4651.
- (34) Wang, X.; Li, M. J.; Yang, S.; Shan, J. J. A Novel Electrochemical Sensor Based on TiO₂-Ti₃C₂T_x/CTAB/Chitosan Composite for the Detection of Nitrite. *Electrochim. Acta* **2020**, *359*, 136938.
- (35) Zhang, J.; Yang, L.; Wang, H. B.; Zhu, G. L.; Wen, H.; Feng, H.; Sun, X.; Guan, X.; Wen, J. Q.; Yao, Y. D.

- In Situ Hydrothermal Growth of TiO₂ Nanoparticles on a Conductive Ti₃C₂T_x MXene Nanosheet: A Synergistically Active Ti-Based Nanohybrid Electrocatalyst for Enhanced N₂ Reduction to NH₃ at Ambient Conditions. *Inorg. Chem.* **2019**, *58*, 5414–5418.
- (36) Fang, Y. F.; Liu, Z. C.; Han, J. R.; Jin, Z. Y.; Han, Y. Q.; Wang, F. X.; Niu, Y. S.; Wu, Y. P.; Xu, Y. H. High-Performance Electrocatalytic Conversion of N₂ to NH₃ Using Oxygen-Vacancy-Rich TiO₂ In Situ Grown on Ti₃C₂T_x MXene. *Adv. Energy Mater.* **2019**, *9*, 1803406.
- (37) Gu, H. S.; Zhang, H.; Zhang, X. Y.; Guo, Y. N.; Yang, L. M.; Wu, H. L.; Mao, N. T. Photocatalytic Properties of Core-Shell Structured Wool-TiO₂ Hybrid Composite Powders, *Catalysts* **2021**, *11*, 12.
- (38) Fleet, M. E.; Harmer, S. L.; Liu, X.; Nesbitt, H. W. Polarized X-ray Absorption Spectroscopy and XPS of TiS₃: S K- and Ti L-Edge XANES and S and Ti 2p XPS. *Surf. Sci.* **2005**, *584*, 133–145.
- (39) Yoshida, T.; Niimi, S.; Yamamoto, M.; Nomoto, T.; Yagi, S. Effective Nitrogen Doping into TiO₂ (N-TiO₂) for Visible Light Response Photocatalysis. *J. Colloid Interf. Sci.* **2015**, *447*, 278–281.
- (40) Chen, J.; Zheng, H. Q.; Zhao, Y.; Que, M. D.; Wang, W. D.; Lei, X. P. Morphology and Photocatalytic Activity of TiO₂/MXene Composites by In-Situ Solvothermal Method. *Ceram. Int.* **2020**, *46*, 20088–20096.
- (41) Kuan, J. L.; Zhang, H.; Gu, H. S.; Zhang, Y. N.; Wu, H. L.; Mao, N. T. Adsorption-Enhanced Photocatalytic Property of Ag-Doped Biochar/g-C₃N₄/TiO₂ Composite by Incorporating Cotton-Based Biochar. *Nanotechnology* **2022**, *33*, 345402.
- (42) Zhao, X. S.; You, Y. Y.; Huang, S. B.; Wu, Y. X.; Ma, Y. Y.; Zhang, G.; Zhang, Z. H. Z-Scheme Photocatalytic Production of Hydrogen Peroxide over Bi₄O₅Br₂/g-C₃N₄ Heterostructure Under Visible Light. *Appl. Catal. B-Environ.* **2020**, *278*, 119251.
- (43) Yang, H.; Mu, J. L.; Chen, X.; Feng, L.; Jia, J.; Wang, J. W. Synthesis, X-ray Crystal Structure and Optical

- Properties of Novel 2,5-Diaryl-1, 3,4-Oxadiazole Derivatives Containing Substituted Pyrazolo[1,5-a] Pyridine Units. *Dyes Pigments* **2011**, *91*, 446–453.
- (44) Smith, J. R.; Amaya, K. R.; Bredemeier, R. T.; Banta, S.; Cropek, D. M. Selective Biomolecular Photocatalytic Decomposition Using Peptide-Modified TiO₂ Nanoparticles. *Appl. Catal. B-Environ.* **2015**, *176*, 315–324.
- (45) Li, Q.; Zhang, J. X.; Wang, Y. F.; Qi, W.; Su, R. X.; He, Z. M. Peptide-Templated Synthesis of TiO₂ Nanofibers with Tunable Photocatalytic Activity. *Chem-Eur. J.* **2018**, *24*, 18123–18129.
- (46) Fard, A. K.; Mckay, G.; Chamoun, R.; Rhadfi, T.; Preud'Homme, H.; Atieh, M. A. Barium Removal from Synthetic Natural and Produced Water Using MXene as Two Dimensional (2-D) Nanosheet Adsorbent. *Chem. Eng. J.* **2017**, *317*, 331–342.
- (47) Chen, W. D.; Zhang, H.; Chen, T. Y.; Yang, L. M.; Wu, H. L.; Tong, Z.; Mao, N. T. TiO₂ Modified Orthocortical and Paracortical Cells Having Enhanced Photocatalytic Degradation and Photoreduction Properties. *Nanotechnology* **2021**, *32*, 025714.
- (48) Ni, S. N.; Qin, H. J.; Wen, J. F.; Li, X. Y.; Li, M.; Tang, T.; Liu, F. C. Burstein-Moss Shift of Lead Halide Perovskite Quantum Dots Induced by Electron Injection from Graphene Oxide. *Appl. Surf. Sci.* **2021**, *545*, 149003.
- (49) Tran, X. M.; Ta, Q. T. H.; Noh, J. S. Unusual Synthesis of Safflower-Shaped TiO₂/Ti₃C₂ Heterostructures Initiated from Two-Dimensional Ti₃C₂ MXene. *Appl. Surf. Sci.* **2021**, *538*, 148023.
- (50) Hou, T. T.; Li, Q.; Zhang, Y. D.; Zhu, W. K.; Yu, K. F.; Wang, S. M.; Xu, Q.; Liang, S. Q.; Wang, L. B. Near-Infrared Light-Driven Photofixation of Nitrogen over Ti₃C₂T_x/TiO₂ Hybrid Structures with Superior Activity and Stability. *Appl. Catal. B-Environ.* **2020**, *273*, 119072.

- (51) Melchers, S.; Schneider, J.; Bahnemann, D. W. Isotopic Studies on the Degradation of Acetaldehyde on Anatase Surfaces. *Catal Today* **2020**, *340*, 318–322.
- (52) Liu, Y.; Wang, X. K.; Chen, B.; Wang, C.; Shen, T. T. Degradation of Azo Dye C.I. Reactive Blue 194 in Water by Sponge Iron in the Presence of Ultrasound. *Environ. Eng. Sci.* **2014**, *31*, 541–547.
- (53) Bansal, P.; Sud, D. Photodegradation of Commercial Dye, CI Reactive Blue 160 Using ZnO Nanopowder: Degradation Pathway and Identification of Intermediates by GC/MS. *Sep. Purif. Technol.* **2012**, *85*, 112–119.
- (54) Rajabinejad, H.; Zoccola, M.; Patrucco, A.; Montarsolo, A.; Rovero, G.; Tonin, C. Physicochemical Properties of Keratin Extracted from Wool by Various Methods. *Text. Res. J.* **2018**, *88*, 2415–2424.
- (55) Li, R. Sun, W. W.; Zhan, C.; Kent, P. R. C.; Jiang, D. E. Interfacial and Electronic Properties of Heterostructures of MXene and Graphene. *Phys. Rev. B* **2019**, *99*, 085429.
- (56) Zeng, F. P.; Feng, X. X.; Chen, X. Y.; Yao, Q.; Miao, Y. L.; Dai, L. J.; Li, Y.; Tang, J. First-Principles Analysis of $\text{Ti}_3\text{C}_2\text{T}_x$ MXene as a Promising Candidate for SF_6 Decomposition Characteristic Components Sensor. *Appl. Surf. Sci.* **2022**, *578*, 152020.
- (57) Zhang, J. Y.; Zhang, H.; Li, W. J.; Yang, L. M.; Wu, H. L.; Mao, N. T. Photocatalytic Properties of A Novel Keratin Char- TiO_2 Composite Films Made Through the Calcination of Wool Keratin Coatings Containing TiO_2 Precursors. *Catalysts* **2021**, *11*, 1366.

TOC GRAPHICS

